

The Birth of a Relativistic Jet Following the Disruption of a Star by a Cosmological Black Hole

Dheeraj Pasham (✉ drreddy@mit.edu)

MIT <https://orcid.org/0000-0003-1386-7861>

Matteo Lucchini

MIT Kavli Institute for Astrophysics and Space Research <https://orcid.org/0000-0002-2235-3347>

Tanmoy Laskar

Department of Astrophysics/IMAPP

Benjamin Gompertz

Institute of Gravitational Wave Astronomy and School of Physics and Astronomy

Shubham Srivastav

Astrophysics Research Centre, School of Mathematics and Physics, Queen's University Belfast

Matt Nicholl

University of Edinburgh

Stephen Smartt

Queen's University Belfast <https://orcid.org/0000-0002-8229-1731>

James Miller-Jones

International Centre for Radio Astronomy Research - Curtin University <https://orcid.org/0000-0003-3124-2814>

Kate Alexander

Northwestern University <https://orcid.org/0000-0002-8297-2473>

Rob Fender

University of Oxford

Graham Smith

University of Birmingham

Michael Fulton

Queen's University Belfast <https://orcid.org/0000-0003-1916-0664>

Gulab Dewangan

Inter-University Centre for Astronomy & Astrophysics

Keith Gendreau

NASA GSFC <https://orcid.org/0000-0001-7115-2819>

Lauren Rhodes

Astrophysics, Department of Physics, University of Oxford

Assaf Horesh

The Hebrew University of Jerusalem <https://orcid.org/0000-0002-5936-1156>

Sjoert van Velzen

Leiden Observatory, Leiden University

Itai Sfaradi

The Hebrew University of Jerusalem <https://orcid.org/0000-0003-0466-3779>

Muryel Guolo

Department of Physics and Astronomy, Johns Hopkins University

N. Castro Segura

Department of Physics & Astronomy. University of Southampton

Aysha Aamer

University of Birmingham

Joseph Anderson

ESO Chile <https://orcid.org/0000-0003-0227-3451>

Iair Arcavi

The School of Physics and Astronomy, Tel Aviv University

Seán Brennan

University College Dublin <https://orcid.org/0000-0003-1325-6235>

Kenneth Chambers

University of Hawaii <https://orcid.org/0000-0001-6965-7789>

Panos Charalampopoulos

DTU Space, National Space Institute, Technical University of Denmark, Elektrovej 327, 2800 Kgs.

<https://orcid.org/0000-0002-0326-6715>

Ting-Wan Chen

Stockholm University <https://orcid.org/0000-0002-1066-6098>

Alejandro Clocchiatti

Pontificia Universidad Católica de Chile

Thomas de Boer

University of Hawaii

Michel Dennefeld

IAP/Paris

Elizabeth Ferrara

University of Maryland

Lluís Galbany

Institute of Space Sciences (ICE, CSIC)

Hua Gao

Institute for Astronomy, University of Hawaii

James Gillanders

Astrophysics Research Centre, School of Mathematics and Physics, Queen's University

<https://orcid.org/0000-0002-8094-6108>

Adelle Goodwin

International Centre for Radio Astronomy Research, Curtin University

Mariusz Gromadzki

University of Warsaw

M Huber

Institute for Astronomy, University of Hawaii

Peter Jonker

Netherland Institute for Space Research <https://orcid.org/0000-0001-5679-0695>

Manasvita Joshi

Research Computing, ITS Division, Northeastern University

Erin Kara

MIT

Thomas Killestein

Department of Physics, University of Warwick <https://orcid.org/0000-0002-0440-9597>

Peter Kosec

MIT Kavli Institute for Astrophysics and Space Research

Daniel Kocevski

NASA/Goddard Space Flight Center

Giorgos Leloudas

Technical University of Denmark <https://orcid.org/0000-0002-8597-0756>

Chien-Cheng Lin

University of Hawaii

Raffaella Margutti

University of California Berkeley

Seppe Mattila

University of Turku

Thomas Moore

Astrophysics Research Centre, School of Mathematics and Physics, Queen's University

Tom\'as M\"uller-Bravo

Institute of Space Sciences (ICE-CSIC)

Chow-Choong Ngeow

Graduate Institute of Astronomy, National Central University

Samantha Oates

University of Birmingham <https://orcid.org/0000-0001-9309-7873>

Francesca Onori

INAF-Osservatorio Astronomico d'Abruzzo, via M. Maggini snc, I-64100

Yen-Chen Pan

Institute of Astronomy, National Central University

Miguel Perez Torres

Instituto de Astrof\'isica de Andaluc\'ia - CSIC <https://orcid.org/0000-0001-5654-0266>

Priyanka Rani

Inter-University Centre for Astronomy & Astrophysics

Ronald Remillard

MIT Kavli Institute

E Ridley

Birmingham Institute for Gravitational Wave Astronomy and School of Physics and Astronomy,
University of Birmingham

Steve Schulze

Stockholm University <https://orcid.org/0000-0001-6797-1889>

Xinyue Sheng

University of Birmingham

Luke Shingles

GSI Helmholtzzentrum f\"ur Schwerionenforschung

Ken Smith

Queen's University Belfast

James Steiner

Smithsonian Astrophysical Observatory

Richard Wainscoat

Institute for Astronomy, University of Hawai'i <https://orcid.org/0000-0002-1341-0952>

Thomas Wevers

European Southern Observatory

Sheng Yang

Oscar Klein Center, Stockholm University <https://orcid.org/0000-0002-2898-6532>

Article

Keywords:

Posted Date: June 10th, 2022

DOI: <https://doi.org/10.21203/rs.3.rs-1700217/v1>

License:  This work is licensed under a Creative Commons Attribution 4.0 International License.

[Read Full License](#)

¹
² The Birth of a Relativistic Jet Following the
Disruption of a Star by a Cosmological Black Hole

³

Dheeraj R. Pasham¹, Matteo Lucchini¹, Tanmoy Laskar²,
Benjamin P. Gompertz^{3,4}, Shubham Srivastav⁵, Matt Nicholl^{3,4},
Stephen J. Smartt⁵, James C. A. Miller-Jones⁶, Kate D. Alexander⁷,
Rob Fender⁸, Graham P. Smith⁴, M. Fulton⁵, Gulab Dewangan⁹, Keith Gendreau¹⁰,
Lauren Rhodes⁸, Assaf Horesh¹¹, Sjoert van Velzen¹², Itai Sfaradi¹¹,
Muryel Guolo¹³, N. Castro Segura¹⁴, Aysha Aamer^{3,4}, Joseph P. Anderson¹⁵,
Iair Arcavi^{16,17}, Seán J. Brennan¹⁸, Kenneth Chambers¹⁹, Panos Charalampopoulos²⁰,
Ting-Wan Chen²¹, A. Clocchiatti^{22,23}, Thomas de Boer¹⁹, Michel Dennefeld²⁴,
Elizabeth Ferrara¹⁰, Lluís Galbany^{25,26}, Hua Gao¹⁹, James H. Gillanders⁵,
Adelle Goodwin⁶, Mariusz Gromadzki²⁷, M Huber¹⁹, Peter G. Jonker^{2,39},
Manasvita Joshi²⁸, Erin Kara¹, Thomas L. Killestein²⁹, Peter Kosec¹,
Daniel Kocevski³⁰, Giorgos Leloudas²⁰, Chien-Cheng Lin¹⁹, Raffaella Margutti³¹,
Seppo Mattila³², Thomas Moore⁵, Tomás Müller-Bravo^{23,24}, Chow-Choong Ngeow³¹,
Samantha Oates^{3,4}, Francesca Onori³⁴, Yen-Chen Pan³¹, Miguel Perez Torres^{35,36},
Priyanka Rani⁹, Ronald Remillard¹, Evan J. Ridley^{3,4}, Steve Schulze²¹,
Xinyue Sheng^{3,4}, Luke Shingles^{5,37}, Ken W. Smith⁵, James Steiner³⁸,
Richard Wainscoat¹⁹, Thomas Wevers¹⁵, Sheng Yang²¹

¹Kavli Institute for Astrophysics and Space Research,

Massachusetts Institute of Technology, Cambridge, MA, USA

²Department of Astrophysics/IMAPP, Radboud University,

PO Box 9010, 6500 GL, The Netherlands

³Institute of Gravitational Wave Astronomy, University of Birmingham, B15 2TT, UK

⁴School of Physics and Astronomy, University of Birmingham, B15 2TT, UK

⁵Astrophysics Research Centre, School of Mathematics and Physics,

Queen's University Belfast, Belfast, BT7 1NN, UK

⁶International Centre for Radio Astronomy Research,

Curtin University, GPO Box U1987, Perth, WA 6845, Australia

⁷Center for Interdisciplinary Exploration and Research in Astrophysics (CIERA) and Department of Physics and Astronomy, Northwestern University, 1800 Sherman Ave, Evanston, IL 60201, USA

⁸Astrophysics, Department of Physics, University of Oxford, Keble Road, Oxford OX1 3RH, UK

⁹The Inter-University Centre for Astronomy and Astrophysics, Pune, India

¹⁰NASA Goddard Space Flight Center, Greenbelt, MD, USA

4

¹¹Racah Institute of Physics, The Hebrew University of Jerusalem, Jerusalem 91904, Israel

¹²Leiden Observatory, Leiden University, Postbus 9513, 2300 RA, Leiden, The Netherlands

¹³Department of Physics and Astronomy, Johns Hopkins University,
3400 N. Charles St., Baltimore MD 21218, USA

¹⁴Department of Physics & Astronomy. University of Southampton,
Southampton SO17 1BJ, UK

¹⁵European Southern Observatory, Alonso de Córdova 3107, Casilla 19, Santiago, Chile

¹⁶The School of Physics and Astronomy, Tel Aviv University, Tel Aviv 69978, Israel

¹⁷CIFAR Azrieli Global Scholars program, CIFAR, Toronto, Canada

¹⁸School of Physics, O'Brien Centre for Science North, University College Dublin,
Belfield, Dublin 4, Ireland

¹⁹Institute for Astronomy, University of Hawaii

²⁰DTU Space, National Space Institute, Technical University of Denmark,
Elektrovej 327, 2800 Kgs. Lyngby, Denmark

²¹The Oskar Klein Centre, Department of Astronomy, Stockholm University,
AlbaNova, SE-10691 Stockholm, Sweden

²²Instituto de Astrofísica, Pontificia Universidad Católica,
Vicuña Mackenna 4860, 7820436 Santiago, Chile

²³Millennium Institute of Astrophysics, Nuncio Monseñor Sótero Sanz 100,
Of. 104, Providencia, 7500000 Santiago, Chile

²⁴IAP/Paris & Sorbonne University

²⁵Institute of Space Sciences (ICE, CSIC), Campus UAB, Carrer de Can Magrans,
s/n, E-08193 Barcelona, Spain.

²⁶Institut d'Estudis Espacials de Catalunya (IEEC), E-08034 Barcelona, Spain

²⁷Astronomical Observatory, University of Warsaw, Al. Ujazdowskie 4,
00-478 Warszawa, Poland

²⁸Research Computing, ITS Division, Northeastern University

²⁹Department of Physics, University of Warwick, Gibbet Hill Road, Coventry CV4 7AL, UK

³⁰NASA Marshall Space Flight Center

³¹Department of Astronomy, University of California, 501 Campbell Hall,
Berkeley, CA 94720, USA

³²TUORLA OBSERVATORY, Department of Physics and Astronomy, University of Turku,
FI-20014 Turku, Finland

5 ³³Graduate Institute of Astronomy, National Central University,
300 Jhongda Road, 32001 Jhongli, Taiwan

34 INAF-Osservatorio Astronomico d'Abruzzo, via M. Maggini snc,
I-64100 Teramo, Italy

35 Instituto de Astrofísica de Andalucía (IAA-CSIC),
Glorieta de la Astronomía s/n, E-18008 Granada, Spain

36 Facultad de Ciencias, Universidad de Zaragoza, Pedro Cerbuna 12, E-50009 Zaragoza, Spain

37 GSI Helmholtzzentrum für Schwerionenforschung, Planckstraße 1,
64291 Darmstadt, Germany

38 Smithsonian Astrophysical Observatory; 60 Garden Street Cambridge, MA 02138, USA

39 SRON, Netherlands Institute for Space Research, Niels Bohrweg 4, 2333 CA Leiden, The Netherlands

6 **The tidal forces of a black hole can rip apart a star that passes too close to it,**
7 **resulting in a stellar Tidal Disruption Event (TDE, (1)). In some such encoun-**
8 **ters, the black hole can launch a powerful relativistic jet (2–6). If this jet fortu-**
9 **itously aligns with our line of sight, the overall brightness is Doppler boosted**
10 **by several orders of magnitude. Consequently, such on-axis relativistic TDEs**
11 **have the potential to unveil cosmological (redshift $z > 1$) quiescent black holes**
12 **and are ideal test beds to understand the radiative mechanisms operating in**
13 **super-Eddington jets. Here, we present multi-wavelength (X-ray, UV, opti-**
14 **cal, and radio) observations of the optically discovered transient AT 2022cmc**
15 **at $z = 1.193$ (7). Its unusual X-ray properties, including a peak observed**
16 **luminosity of $\gtrsim 10^{48}$ erg s⁻¹, systematic variability on timescales as short as**
17 **1000 seconds, and overall duration lasting more than 30 days in the rest-frame**
18 **are traits associated with relativistic TDEs. This makes AT 2022cmc only the**
19 **fourth member of this rare class and the first one identified in the optical and**
20 **with well-sampled optical data. The X-ray to radio spectral energy distri-**
21 **butions spanning 5–50 days after discovery can be explained as synchrotron**

22 **emission from a relativistic jet (radio), synchrotron self-Compton (X-rays),**
23 **and thermal emission similar to that seen in low-redshift TDEs (UV/optical).**
24 **Our modeling implies a beamed, highly relativistic jet akin to blazars (e.g.,**
25 **(8, 9)) but requires extreme matter-domination, i.e, high ratio of electron-to-**
26 **magnetic field energy densities in the jet, and challenges our theoretical under-**
27 **standing of jets. This work provides one of the best multi-wavelength datasets**
28 **of a newborn relativistic jet to date and will be invaluable for testing more**
29 **sophisticated jet models, and for identifying more such events in transient sur-**
30 **veys.**

31 AT 2022cmc was discovered in the optical waveband by the Zwicky Transient Facility
32 (ZTF; (10)) on 11 February 2022 as a fast-evolving transient, and was publicly reported to the
33 Gamma-ray Coordination Network (GCN) on 14 February 2022 (7). We confirmed the rapid
34 evolution of this transient in the Asteroid Terrestrial-impact Last Alert System (ATLAS) survey
35 data with a non-detection 24 hrs before the ZTF discovery and a subsequent decline of 0.6 mag-
36 nitudes per day (11). A radio counterpart was identified in Karl G. Jansky Very Large Array
37 (VLA) observations on 15 February 2022 (12). While the optical spectrum taken on 16 February
38 2022 revealed a featureless continuum (13), spectral features were detected in subsequent spec-
39 tra taken one day later with the European Southern Observatory’s (ESO) Very Large Telescope
40 (VLT; (14)) and Keck/DEIMOS (15). In particular, the detection of [OIII] λ 5007 emission and
41 CaII, MgII and FeII absorption lines yielded a redshift measurement of $z = 1.193$ (14, 15). Our
42 follow-up X-ray (0.3–5 keV) observations with the Neutron star Interior Composition ExploreR
43 (NICER) on 16 February 2022 revealed a luminous X-ray counterpart (16). We also triggered
44 additional multi-wavelength observations with numerous facilities, including *AstroSat* and The
45 Neil Gehrels *Swift* Observatory (*Swift*) in the X-rays and the UV (see Extended Data Figures 1
46 and 2). We obtained an optical spectrum with ESO/VLT (Extended Data Figure 3) and imag-

47 ing with several optical telescopes. In the radio band, we acquired multi-frequency data with
48 the VLA, the Arcminute Microkelvin Imager-Large Array (AMI-LA) and the European Very
49 Long Baseline Interferometry (VLBI) Network (EVN; see “Observations and Data Analysis” in
50 Methods for details on these observations). We adopt Modified Julian Date (MJD) 59621.4458
51 (the discovery epoch) as the reference time throughout the paper and all relative times are in the
52 observer frame unless otherwise mentioned.

53 AT 2022cmc’s most striking property is its high isotropic peak X-ray luminosity of \gtrsim
54 10^{48} erg s $^{-1}$ (orange data points in panel (a) of Figure 1). High apparent luminosity can be
55 caused by gravitational lensing, however this contributes no more than a 10% enhancement for
56 AT 2022cmc (see “Estimate of gravitational lens magnification by a foreground structure” in
57 Methods). AT 2022cmc’s second compelling aspect is its rapid X-ray variability over a wide
58 range of timescales: during the weeks after initial optical discovery, it showed variability on
59 timescales ranging from 1000 s to many days (see panels (a)–(d) of Figure 1, Extended Data
60 Figure 4, and “Shortest X-ray variability timescale” in Methods). The X-ray spectrum is gener-
61 ally consistent with a simple power law model with the best-fit photon index varying between
62 1.3–1.9 (Extended Data Figure 2 and Extended Data Table 2). There are intermittent rapid
63 flares during which the X-ray spectrum deviates from a power law model (see “ γ -rays and X-
64 rays/NICER” in Methods). AT 2022cmc’s observed optical and UV light curves exhibit three
65 phases after reaching their peaks: an early slow decline* phase at \lesssim 3.1 days with a decline
66 rate $\alpha \approx -0.5$ steepening further to $\alpha \approx -2.5$ at \approx 6.4 days, followed by a shallow decline
67 ($\alpha \approx -0.3$) at \gtrsim 6.4 days (see Figure 2). An optical spectrum taken at \approx 15 days shows a fea-
68 tureless blue continuum, which can be fit using a thermal model with a rest-frame temperature
69 $\approx 3 \times 10^4$ K (see Extended Data Figure 3). The 15 GHz flux density, on the other hand, has been
70 rising monotonically with time at \gtrsim 10 days (see Figure 2). The radio spectrum appears to be

*We use the convention, $F_\nu(\nu) \propto t^\alpha \nu^\beta$ throughout, where F_ν is the flux per unit frequency, ν is the observed frequency, α is the temporal decay rate, and β is the spectral index.

71 consistent with the standard synchrotron self-absorption process from a single-emitting region
72 (e.g., see (17)).

73 AT 2022cmc’s high apparent X-ray energy output, extreme luminosity variations (a factor
74 of ~ 500 over a few weeks; see Figure 2 gray and black points) and fast variability requires
75 an active central engine. Such an engine can be naturally explained by an extreme accre-
76 tion episode onto a black hole which could be due to a stellar tidal disruption (1). Indeed,
77 among transients, AT 2022cmc’s apparent X-ray luminosity and evolution are only comparable
78 to Sw J1644+57 (e.g., (3)), Sw J2058.4+0516 (e.g., (18, 19)) and Sw J1112.2-8238 (20), the
79 three TDEs with relativistic jets. AT 2022cmc’s thermal optical emission with temperature of
80 $\sim 2.3 \times 10^4$ K is often seen in low-redshift ($z \lesssim 0.2$) TDEs (21). The high optical/UV luminosity
81 of $\approx 2 \times 10^{45}$ erg s $^{-1}$ at day 15-16 post-discovery (Figure 3) is only comparable to the extreme
82 TDE candidate ASASSN-15lh (22). Based on the rich literature on accretion-driven outbursts
83 from stellar-mass black holes in X-ray binaries, we now know that accretion and consequently
84 related ejection can lead to variability on a wide range of timescales (see references in (23)).
85 Thus, accretion/ejection following a tidal disruption could also naturally explain AT 2022cmc’s
86 observed flux variability over a wide range of timescales.

87 Given the similar X-ray luminosity and variability to Sw J1644+57, the best-studied TDE
88 with a relativistic jet, we modelled AT 2022cmc’s data under the jet paradigm. In a standard jet
89 scenario, the radio through infrared/optical/UV data is dominated by non-thermal synchrotron
90 emission (2, 24). However, extrapolating AT 2022cmc’s radio/optical/UV data to higher fre-
91 quencies does not provide emission consistent with the observed X-ray flux (see “Preliminary
92 Considerations” in Methods and Extended Data Figure 6), suggesting that the high energy emis-
93 sion originates from a second component. Similar to blazars, this second component could nat-
94 urally arise from inverse Compton scattering of either local synchrotron photons (synchrotron
95 self-Compton, or SSC for brevity), or photons originating outside of the jet (external Compton,

96 or EC). In both cases, the photons would interact with the electrons in the jet. Therefore, we in-
97 vestigated these scenarios by fitting three observed time-averaged spectral energy distributions
98 (SEDs) with good multi-wavelength coverage (days 15-16, 25-27, and 41-46) with a simple jet
99 model, consisting of a spherical, homogeneous, emitting region, similar to the approach com-
100 monly used to infer the properties of the emitting region in blazars (8, 25, 26). The rapid X-ray
101 variability on tens of minutes timescale and self-absorbed radio spectrum indicate that the ob-
102 served radio and X-ray emission originate from a compact region rather than in an extended
103 outflow, further motivating our single-zone approximation.

104 We tested two emission models, one in which the only radiative mechanisms considered are
105 synchrotron and SSC (model 1), and one including EC of thermal photons originating outside
106 of the jet (model 2). Model 1 (the synchrotron+SSC model), shown in Figure 3, provides
107 an acceptable fit to the radio through the X-ray SEDs ($\chi^2/\text{d.o.f.} = 2.2$), albeit with extreme
108 parameters (see below); model 2 on the other hand is disfavored because it cannot explain
109 the radio flux, while still resulting in similarly extreme parameters (see “Modeling results” in
110 Methods). The best-fitting parameters for both models are reported in Extended Data Table 3.
111 We caution that these numbers could change significantly with a more complex and physical
112 model, and the fits presented here purely constitute a check that the data is consistent with the
113 emission from a relativistic jet.

114 The main trend emerging from model 1 is that the jet has to be very powerful ($\approx 10^{46-47}$
115 erg s^{-1} , depending on its composition) and strongly beamed: the Doppler factor is $\delta = [\Gamma_j(1 -$
116 $\beta_j \cos(\theta)]^{-1} \sim 100$, where Γ_j is the jet bulk Lorentz factor, β_j the corresponding speed in units
117 of the speed of light, and θ is the jet viewing angle. On the other hand, model 2 requires
118 somewhat lower jet power ($\approx 10^{45} \text{ erg s}^{-1}$), and a smaller Doppler factor $\delta \approx 10$. Under the
119 jet paradigm, the observed X-rays and their variability arise from within the jet; as a result,
120 a size constraint can be compared to the observed variability timescale in order to check for

121 consistency. Based on a simple causality argument, we require the size of the emitting region
122 to be smaller than the minimum variability timescale \times speed of light \times Doppler factor ≈ 1000 s
123 $\times 3 \times 10^{10} \times \delta$ cm $\approx 3 \times 10^{13} \times \delta$ cm for our case, where the factor δ accounts for relativistic
124 beaming (27). The emitting region inferred has an estimated radius of $\approx 10^{15-16}$ cm from
125 model 1 and $\approx 10^{14}$ cm from model 2. Both of these estimates are consistent with the hour-
126 long variability timescale observed by *NICER* but are only marginally consistent with ~ 1000 s
127 X-ray variations. Such rapid variability has also been observed in some extreme blazar flares
128 (e.g., (28, 29)), and is inconsistent with the simple homogeneous, time-independent single-zone
129 model presented here. Instead, it can be reproduced using a complex in-homogeneous, time-
130 dependent model (30). However, applying such a model to AT 2022cmc is beyond the scope of
131 this work.

132 Both models 1 and 2 require a strong SSC contribution to match the X-ray flux. In order
133 for this to happen, we require a strongly matter-dominated jet, i.e., most of the power is carried
134 by the electrons and protons within the jet, rather than by the magnetic field. Such a matter
135 dominated flow is in tension with the common theoretical paradigm that jets are magnetically-
136 dominated at their launching point, and then accelerate by turning the magnetic field into bulk
137 kinetic energy until they reach rough equipartition (31, 32). These issues are also often encoun-
138 tered when modelling blazar jets with a dominant SSC component, (8, 9), as well as M87 (33),
139 and likely points at the need for more complex models. A schematic of our proposed, albeit
140 simple, model (synchrotron+SSC+thermal optical/UV) is shown in Figure 4.

141 Finally, our SED models imply that the underlying physics in AT 2022cmc’s jet maybe dis-
142 tinct compared to Sw J1644+57 and Sw J2058+05, as in those sources SSC cannot produce the
143 observed X-ray emission (34). In Sw J1644+57 it has been argued that the X-ray originate from
144 a corona/base of a jet through external inverse Compton scattering by a photon field coming
145 from either the disk (e.g., (3)) or from the disk wind (e.g., (34)). This external inverse Compton

¹⁴⁶ model has also been successfully applied to Sw J2058+05 (35). Instead, in AT 2022cmc EC
¹⁴⁷ cannot explain the observed X-rays (see “Modeling results” in Methods), and thus its high en-
¹⁴⁸ ergy emission appears to be driven by different mechanisms compared to previous relativistic
¹⁴⁹ TDEs.

¹⁵⁰ While our models provide strong evidence that the multi-wavelength emission of AT 2022cmc
¹⁵¹ is powered by a relativistic jet, they also show that a more complex model is required to probe
¹⁵² the physics of the jet self-consistently. The data presented in this paper provide an unprece-
¹⁵³ dented opportunity to explore detailed jet physics at extreme mass accretion rates.

¹⁵⁴ As a relativistic jet is able to explain the multi-wavelength properties of AT 2022cmc, we
¹⁵⁵ now investigate the plausible mass of the black hole engine. At the low mass end, $\sim 10 M_{\odot}$,
¹⁵⁶ the most powerful known jets are launched following Gamma Ray Bursts (GRBs). A GRB
¹⁵⁷ afterglow interpretation can be ruled out due to the: 1) unusually high X-ray luminosity, 2)
¹⁵⁸ fast variability out to weeks after discovery, 3) overall duration of AT 2022cmc, and 4) non-
¹⁵⁹ synchrotron SED (see “Arguments against a GRB afterglow” in Methods for a more thor-
¹⁶⁰ ough/detailed discussion). We disfavour a blazar flare/outburst for three reasons. First, the
¹⁶¹ light curves of blazar flares show stochastic variability on top of a fairly constant, low flux
¹⁶² (e.g. (30)), while AT 2022cmc shows a smooth decay structure typical of transients powered by
¹⁶³ a sudden (and possibly subsequently sustained) deposition of energy. Second, all blazar classes
¹⁶⁴ have a flat radio spectrum, $F(\nu) \propto \nu^0$, while AT 2022cmc exhibits a strongly self-absorbed
¹⁶⁵ spectrum with $F(\nu) \propto \nu^2$. Finally, a large amplitude optical brightness enhancement of ~ 4
¹⁶⁶ magnitudes (see “Constraints on host luminosity” in Methods and supplementary data) is un-
¹⁶⁷ usual for blazars (e.g., compare with (30)). In addition to this, there is no gamma-ray source
¹⁶⁸ detected by Fermi/LAT within 1° diameter from AT 2022cmc. However, both an intermediate-
¹⁶⁹ mass black hole weighing a few $\times (10^{2-5}) M_{\odot}$ disrupting a white dwarf and a supermassive
¹⁷⁰ black hole (a few $\times 10^{6-8}$) disrupting a solar type star remain as possible scenarios for powering

¹⁷¹ AT 2022cmc. The observed high apparent X-ray luminosity implies that the emission is highly
¹⁷² super-Eddington in both of these cases.

¹⁷³ While non-relativistic TDEs are now routinely discovered (roughly one every few weeks)
¹⁷⁴ in the nearby Universe (redshift, $z \lesssim 0.2$) (21, 36), Doppler-boosted TDEs such as AT 2022cmc
¹⁷⁵ can push the redshift barrier as they are orders of magnitude more luminous. AT 2022cmc's
¹⁷⁶ multi-wavelength properties are consistent with a TDE with a relativistic jet closely aligned
¹⁷⁷ with our line of sight. This makes AT 2022cmc the farthest TDE known to-date. It is also the
¹⁷⁸ first relativistic TDE to be identified in over 11 years (6), and the first such event to be identified
¹⁷⁹ by an optical sky survey. All these factors bolster the exciting prospect of unveiling $z > 1$ TDEs
¹⁸⁰ and consequently black holes in the upcoming era of *LSST/Rubin* observatory (37).

181 **References**

- 182 1. M. J. Rees, *Nature* **333**, 523 (1988).
- 183 2. D. Giannios, B. D. Metzger, *Mon. Not. R. Astron. Soc.* **416**, 2102 (2011).
- 184 3. J. S. Bloom, *et al.*, *Science* **333**, 203 (2011).
- 185 4. A. J. Levan, *et al.*, *Science* **333**, 199 (2011).
- 186 5. S. B. Cenko, *et al.*, *Astrophys. J.* **753**, 77 (2012).
- 187 6. G. C. Brown, *et al.*, *Mon. Not. R. Astron. Soc.* **452**, 4297 (2015).
- 188 7. I. Andreoni, *et al.*, *GRB Coordinates Network* **31590**, 1 (2022).
- 189 8. F. Tavecchio, G. Ghisellini, *Mon. Not. R. Astron. Soc.* **456**, 2374 (2016).
- 190 9. L. Costamante, *et al.*, *Mon. Not. R. Astron. Soc.* **477**, 4257 (2018).
- 191 10. E. C. Bellm, *et al.*, *Publ. Astron. Soc. Pac.* **131**, 018002 (2019).
- 192 11. M. Fulton, *et al.*, *Transient Name Server AstroNote* **40**, 1 (2022).
- 193 12. D. A. Perley, *GRB Coordinates Network* **31592**, 1 (2022).
- 194 13. T. Ahumada, *et al.*, *GRB Coordinates Network* **31595**, 1 (2022).
- 195 14. M. J. Lundquist, C. A. Alvarez, J. O'Meara, *GRB Coordinates Network* **31612**, 1 (2022).
- 196 15. N. R. Tanvir, *et al.*, *GRB Coordinates Network* **31602**, 1 (2022).
- 197 16. D. Pasham, K. Gendreau, Z. Arzoumanian, B. Cenko, *GRB Coordinates Network* **31601**,
198 1 (2022).

199 17. R. Barniol Duran, E. Nakar, T. Piran, *Astrophys. J.* **772**, 78 (2013).

200 18. S. B. Cenko, *et al.*, *Astrophys. J.* **753**, 77 (2012).

201 19. D. R. Pasham, *et al.*, *Astrophys. J.* **805**, 68 (2015).

202 20. G. C. Brown, *et al.*, *Mon. Not. R. Astron. Soc.* **452**, 4297 (2015).

203 21. S. van Velzen, *et al.*, *Astrophys. J.* **908**, 4 (2021).

204 22. G. Leloudas, *et al.*, *Nature Astronomy* **1**, 0002 (2016).

205 23. J. E. McClintock, R. A. Remillard, *Compact stellar X-ray sources* (2006), vol. 39, pp.
206 157–213.

207 24. G. E. Romero, M. Boettcher, S. Markoff, F. Tavecchio, *Space Sci. Rev.* **207**, 5 (2017).

208 25. G. Ghisellini, F. Tavecchio, *Mon. Not. R. Astron. Soc.* **397**, 985 (2009).

209 26. M. Böttcher, A. Reimer, K. Sweeney, A. Prakash, *Astrophys. J.* **768**, 54 (2013).

210 27. G. Ghisellini, *Radiative Processes in High Energy Astrophysics*, vol. 873 (2013).

211 28. F. Aharonian, *et al.*, *Astrophys. J.* **664**, L71 (2007).

212 29. M. Hayashida, *et al.*, *Astrophys. J.* **807**, 79 (2015).

213 30. C. M. Raiteri, *et al.*, *Nature* **552**, 374 (2017).

214 31. J. C. McKinney, *Mon. Not. R. Astron. Soc.* **368**, 1561 (2006).

215 32. K. Chatterjee, M. Liska, A. Tchekhovskoy, S. B. Markoff, *Mon. Not. R. Astron. Soc.* **in**
216 **press** (2019).

217 33. EHT MWL Science Working Group, *et al.*, *Astrophys. J.* **911**, L11 (2021).

218 34. P. Crumley, *et al.*, *Mon. Not. R. Astron. Soc.* **460**, 396 (2016).

219 35. W. Lu, P. Kumar, *Mon. Not. R. Astron. Soc.* **458**, 1071 (2016).

220 36. E. Hammerstein, *et al.*, *arXiv e-prints* p. arXiv:2203.01461 (2022).

221 37. K. Bricman, A. Gomboc, *Astrophys. J.* **890**, 73 (2020).

222 38. B. P. Gompertz, A. S. Fruchter, A. Pe'er, *Astrophys. J.* **866**, 162 (2018).

223 39. M. Nicholl, *et al.*, *Mon. Not. R. Astron. Soc.* **499**, 482 (2020).

224 40. T. Piran, G. Svirski, J. Krolik, R. M. Cheng, H. Shiokawa, *Astrophys. J.* **806**, 164 (2015).

225 41. Planck Collaboration, *et al.*, *Astron. Astrophys.* **641**, A6 (2020).

226 42. K. P. Singh, *et al.*, *Journal of Astrophysics and Astronomy* **38**, 29 (2017).

227 43. D. R. Pasham, *et al.*, *Nature Astronomy* **6**, 249 (2021).

228 44. J. S. Kaastra, J. A. M. Bleeker, *Astron. Astrophys.* **587**, A151 (2016).

229 45. K. A. Arnaud, *Astronomical Data Analysis Software and Systems V*, G. H. Jacoby,
230 J. Barnes, eds. (1996), vol. 101 of *Astronomical Society of the Pacific Conference Series*,
231 p. 17.

232 46. HI4PI Collaboration, *et al.*, *Astron. Astrophys.* **594**, A116 (2016).

233 47. R. A. Remillard, *et al.*, *Astron. J.* **163**, 130 (2022).

234 48. B. Cenko, *GRB Coordinates Network* **31603**, 1 (2022).

235 49. P. A. Evans, *et al.*, *Astron. Astrophys.* **469**, 379 (2007).

236 50. P. A. Evans, *et al.*, *Mon. Not. R. Astron. Soc.* **397**, 1177 (2009).

237 51. J. S. Bloom, D. A. Frail, R. Sari, *Astron. J.* **121**, 2879 (2001).

238 52. K. W. Smith, *et al.*, *Research Notes of the American Astronomical Society* **3**, 26 (2019).

239 53. F. J. Masci, *et al.*, *Publ. Astron. Soc. Pac.* **131**, 018003 (2019).

240 54. E. F. Schlafly, D. P. Finkbeiner, *Astrophys. J.* **737**, 103 (2011).

241 55. J. L. Tonry, *et al.*, *Publ. Astron. Soc. Pac.* **130**, 064505 (2018).

242 56. K. W. Smith, *et al.*, *Publ. Astron. Soc. Pac.* **132**, 085002 (2020).

243 57. L. Shingles, *et al.*, *Transient Name Server AstroNote* **7**, 1 (2021).

244 58. S. J. Smartt, *et al.*, *Astron. Astrophys.* **579**, A40 (2015).

245 59. M. Nicholl, photometry-sans-frustration: Interactive python wrapper for point-spread fit-
246 ting (psf) photometry.

247 60. K. C. Chambers, *et al.*, *ArXiv e-prints* (2016).

248 61. E. A. Magnier, *et al.*, *Astrophys. J. Suppl.* **251**, 5 (2020).

249 62. T. W. Chen, *et al.*, *Transient Name Server AstroNote* **92**, 1 (2021).

250 63. S. J. Brennan, M. Fraser, *arXiv e-prints* p. arXiv:2201.02635 (2022).

251 64. T. W. Chen, *et al.*, *Transient Name Server AstroNote* **39**, 1 (2022).

252 65. D. A. Perley, *GRB Coordinates Network* **31592**, 1 (2022).

253 66. N. Pankov, *et al.*, *GRB Coordinates Network* **31593**, 1 (2022).

254 67. D. A. Perley, *GRB Coordinates Network* **31594**, 1 (2022).

255 68. H. Kumar, *et al.*, *GRB Coordinates Network* **31597**, 1 (2022).

256 69. Pankov, *et al.*, *GRB Coordinates Network* **31625**, 1 (2022).

257 70. J. Freeburn, *et al.*, *GRB Coordinates Network* **31647**, 1 (2022).

258 71. N. Pankov, A. Pozanenko, E. Klunko, S. Belkin, GRB IKI FuN, *GRB Coordinates Net-*
259 *work* **31652**, 1 (2022).

260 72. S. B. Cenko, I. Andreoni, M. Coughlin, *GRB Coordinates Network* **31729**, 1 (2022).

261 73. N. Pankov, *et al.*, *GRB Coordinates Network* **31798**, 1 (2022).

262 74. Dimple, *et al.*, *GRB Coordinates Network* **31805**, 1 (2022).

263 75. N. Pankov, *et al.*, *GRB Coordinates Network* **31846**, 1 (2022).

264 76. P. W. A. Roming, *et al.*, *Space Sci. Rev.* **120**, 95 (2005).

265 77. L. Bianchi, *et al.*, *Ap&SS* **335**, 161 (2011).

266 78. S. N. Tandon, *et al.*, *Astron. J.* **154**, 128 (2017).

267 79. S. N. Tandon, *et al.*, *Astron. J.* **159**, 158 (2020).

268 80. K. P. Singh, *et al.*, *SPIE* (2014), vol. 9144 of *Society of Photo-Optical Instrumentation*
269 *Engineers (SPIE) Conference Series*, p. 91441S.

270 81. J. E. Postma, D. Leahy, *Publ. Astron. Soc. Pac.* **129**, 115002 (2017).

271 82. J. Vernet, *et al.*, *Astron. Astrophys.* **536**, A105 (2011).

272 83. J. Selsing, *et al.*, *Astron. Astrophys.* **623**, A92 (2019).

273 84. P. G. van Dokkum, *Publ. Astron. Soc. Pac.* **113**, 1420 (2001).

274 85. P. Goldoni, *et al.*, *Society of Photo-Optical Instrumentation Engineers (SPIE) Conference*
275 *Series*, I. S. McLean, M. Iye, eds. (2006), vol. 6269 of *Society of Photo-Optical Instru-*
276 *mentation Engineers (SPIE) Conference Series*, p. 62692K.

277 86. A. Modigliani, *et al.*, *Observatory Operations: Strategies, Processes, and Systems III*,
278 D. R. Silva, A. B. Peck, B. T. Soifer, eds. (2010), vol. 7737 of *Society of Photo-Optical*
279 *Instrumentation Engineers (SPIE) Conference Series*, p. 773728.

280 87. S. van Velzen, *et al.*, *Astrophys. J.* **908**, 4 (2021).

281 88. J. P. McMullin, B. Waters, D. Schiebel, W. Young, K. Golap, *Astronomical Data Anal-*
282 *ysis Software and Systems XVI*, R. A. Shaw, F. Hill, D. J. Bell, eds. (2007), vol. 376 of
283 *Astronomical Society of the Pacific Conference Series*, p. 127.

284 89. J. T. Zwart, *et al.*, *MNRAS* **391**, 1545 (2008).

285 90. J. Hickish, *et al.*, *Mon. Not. R. Astron. Soc.* **475**, 5677 (2018).

286 91. G. E. Anderson, *et al.*, *Mon. Not. R. Astron. Soc.* **473**, 1512 (2018).

287 92. I. Sfaradi, *et al.*, *GRB Coordinates Network* **31667**, 1 (2022).

288 93. D. Dobie, *et al.*, *GRB Coordinates Network* **31665**, 1 (2022).

289 94. K. Alexander, *et al.*, *The Astronomer's Telegram* **15269**, 1 (2022).

290 95. E. W. Greisen, *Information Handling in Astronomy - Historical Vistas*, A. Heck, ed.
291 (2003), vol. 285 of *Astrophysics and Space Science Library*, p. 109.

292 96. D. A. Leahy, *et al.*, *Astrophys. J.* **266**, 160 (1983).

293 97. Fermi GBM Team, *GRB Coordinates Network* **31570**, 1 (2022).

294 98. A. Ridnaia, *et al.*, *GRB Coordinates Network* **31584**, 1 (2022).

295 99. S. E. Woosley, *Astrophys. J.* **405**, 273 (1993).

296 100. A. I. MacFadyen, S. E. Woosley, *Astrophys. J.* **524**, 262 (1999).

297 101. P. Kumar, B. Zhang, *PhysRep* **561**, 1 (2015).

298 102. R. D. Blandford, C. F. McKee, *Physics of Fluids* **19**, 1130 (1976).

299 103. B. Paczynski, *Astrophys. J.* **308**, L43 (1986).

300 104. M. J. Rees, P. Meszaros, *Mon. Not. R. Astron. Soc.* **258**, 41 (1992).

301 105. R. Sari, T. Piran, R. Narayan, *Astrophys. J.* **497**, L17 (1998).

302 106. J. Granot, R. Sari, *Astrophys. J.* **568**, 820 (2002).

303 107. A. Pe'er, *Advances in Astronomy* **2015**, 907321 (2015).

304 108. S. Kobayashi, T. Piran, R. Sari, *Astrophys. J.* **490**, 92 (1997).

305 109. A. J. Levan, *et al.*, *Astrophys. J.* **781**, 13 (2014).

306 110. B.-B. Zhang, B. Zhang, K. Murase, V. Connaughton, M. S. Briggs, *Astrophys. J.* **787**, 66 (2014).

308 111. C. J. Saxton, R. Soria, K. Wu, N. P. M. Kuin, *Mon. Not. R. Astron. Soc.* **422**, 1625 (2012).

309 112. D. R. Pasham, *et al.*, *Astrophys. J.* **805**, 68 (2015).

310 113. R. Barniol Duran, E. Nakar, T. Piran, *Astrophys. J.* **772**, 78 (2013).

311 114. D. N. Burrows, *et al.*, *Nature* **476**, 421 (2011).

312 115. M. Lucchini, *et al.*, *arXiv e-prints* p. arXiv:2108.12011 (2021).

313 116. A. B. Pushkarev, Y. Y. Kovalev, M. L. Lister, T. Savolainen, *Astron. Astrophys.* **507**, L33
314 (2009).

315 117. J. C. Houck, L. A. Denicola, *Astronomical Data Analysis Software and Systems IX*,
316 N. Manset, C. Veillet, D. Crabtree, eds. (2000), vol. 216 of *Astronomical Society of the*
317 *Pacific Conference Series*, p. 591.

318 118. D. Foreman-Mackey, D. W. Hogg, D. Lang, J. Goodman, *Publications of the Astronomical*
319 *Society of the Pacific* **125**, 306 (2013).

320 119. F. Tavecchio, L. Maraschi, G. Ghisellini, *Astrophys. J.* **509**, 608 (1998).

321 120. Z. L. Wen, J. L. Han, *Astrophys. J.* **807**, 178 (2015).

322 121. S. L. Mulroy, *et al.*, *Mon. Not. R. Astron. Soc.* **484**, 60 (2019).

323 122. C. O. Wright, T. G. Brainerd, *Astrophys. J.* **534**, 34 (2000).

324 123. Y.-T. Lin, J. J. Mohr, S. A. Stanford, *Astrophys. J.* **610**, 745 (2004).

325 124. J. Richard, *et al.*, *Mon. Not. R. Astron. Soc.* **404**, 325 (2010).

326 125. G. P. Smith, *et al.*, *arXiv e-prints* p. arXiv:2204.12977 (2022).

327 126. A. Dey, *et al.*, *Astron. J.* **157**, 168 (2019).

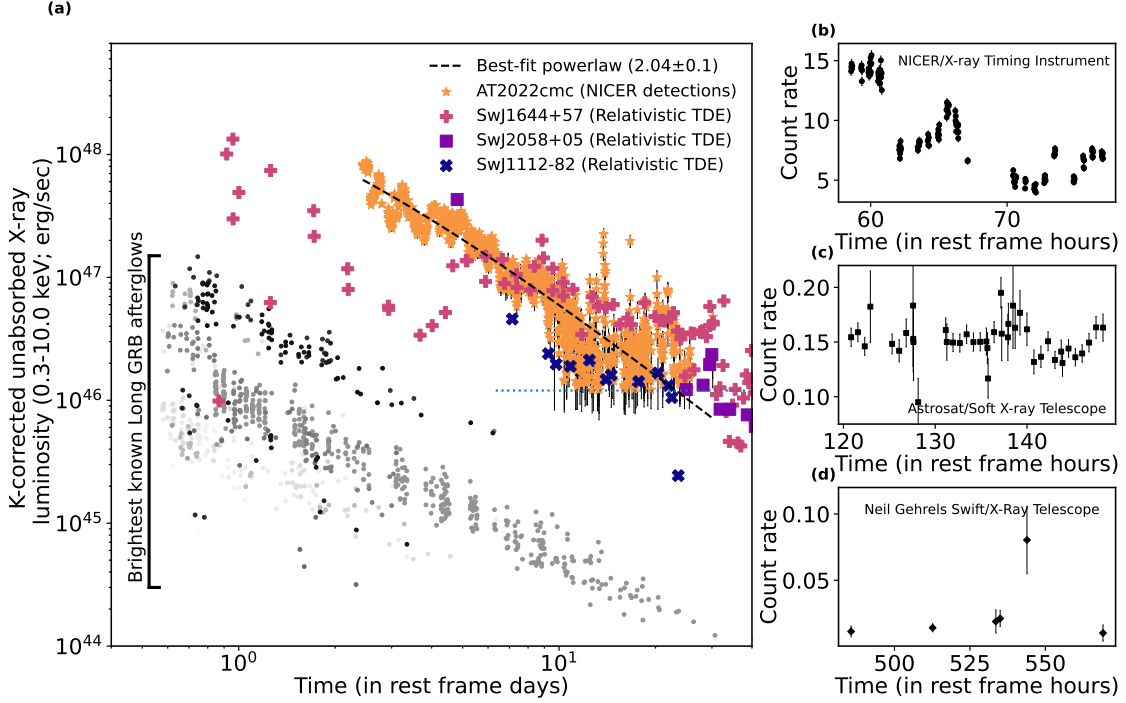


Figure 1: AT 2022cmc’s X-ray evolution on various timescales at different epochs. (a) **AT 2022cmc’s absorption-corrected and k-corrected 0.3-10 keV X-ray luminosity (filled orange stars) in comparison to the most luminous known X-ray transients.** The filled circles with different shades of grey are a sample of the most luminous GRB X-ray afterglows known (38). Only data past 50,000 rest-frame seconds is shown to highlight the late time emission from these afterglows. AT 2022cmc is significantly more luminous than any known GRB afterglow and its X-ray luminosity is only comparable to previously-known relativistic jetted TDEs Sw J1644+57 (filled green crosses), Sw J2058+05 (filled cyan squares) and Sw J1112-82 (filled purple Xs). The dotted horizontal blue line at 1.2×10^{46} erg s $^{-1}$ is an estimate of NICER’s background-limited sensitivity limit for sources at $z = 1.193$. See “GRB and TDE Comparison Data” in Methods for a description of the comparison sample used in this Figure. (b) **AT 2022cmc’s sample NICER (0.3-5 keV) light curve** highlighting variability on hours timescale (also see Extended Data Figure 4). (c) **AT 2022cmc’s Astrosat (0.5-7 keV) light curve showing variability on hours timescale.** (d) **AT 2022cmc’s Swift X-ray (0.3-8 keV) light curve** highlighting a flare more than 3 weeks (in rest-frame) after initial discovery. All the light curves are background-corrected. In panels (b)-(d), background-corrected count rates (counts s $^{-1}$) vs time in rest frame hours since MJD 59621.4458 are shown. These data are provided as supplementary files.

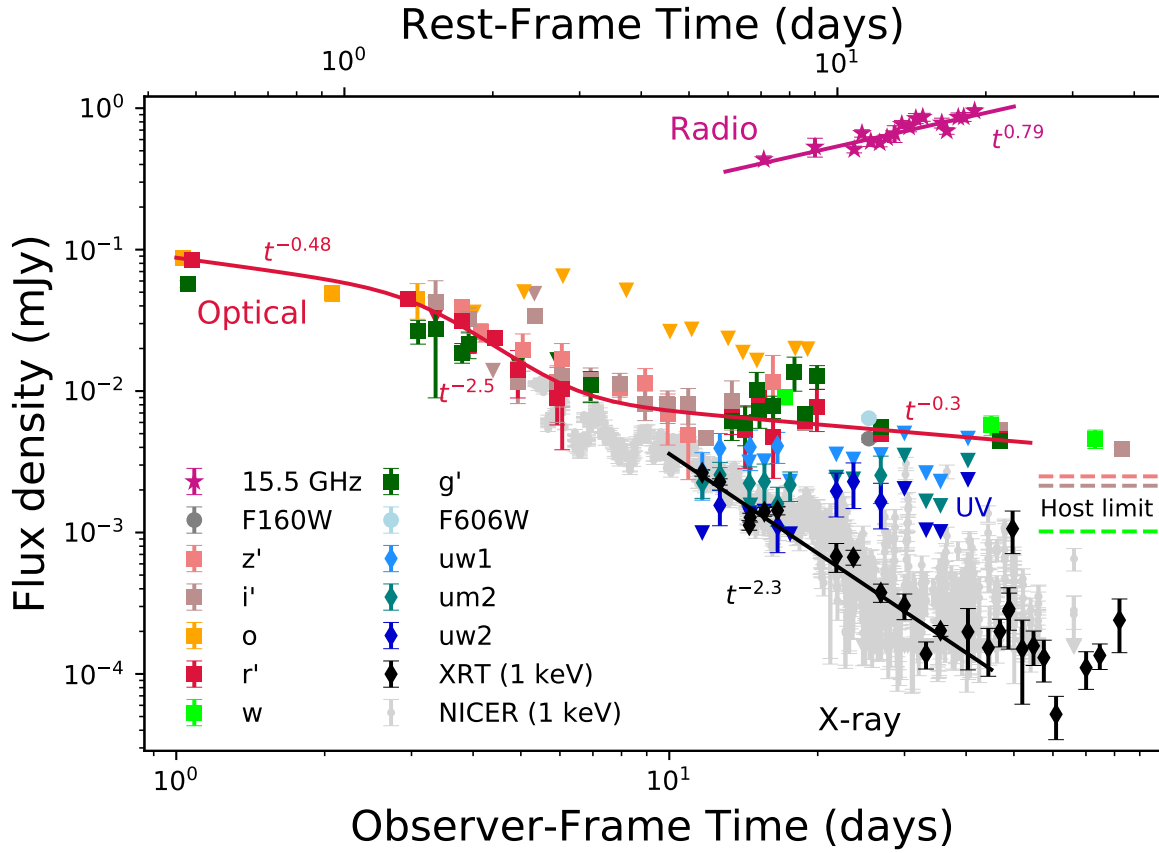


Figure 2: **NICER** (small grey points), **Swift/XRT** and **UVOT** (diamonds), **HST** (circles), **ground-based optical** (squares), and **radio** (stars) light curves of AT 2022cmc spanning from ≈ 1 –83 days after discovery, together with single / smoothly broken power-law models fit to the **Swift/XRT** (black), r' -band (red) and 15 GHz (violet) light curves with the corresponding best-fit indices indicated. The optical light curve exhibits a steep decay at ≈ 1 –3 days in the rest frame, followed by a plateau, during which the radio light curve is seen to rise. Dashed lines indicate w , i , and z -band upper limits on underlying host emission obtained from deep stacks of PanSTARRS pre-discovery images (see “Constraints on host luminosity” and Extended Data Figure 5 in Methods). Upper limits are indicated by inverted triangles. All photometry presented in this figure is corrected for Galactic extinction, and is available as a supplementary file (Extended Data Table 1).

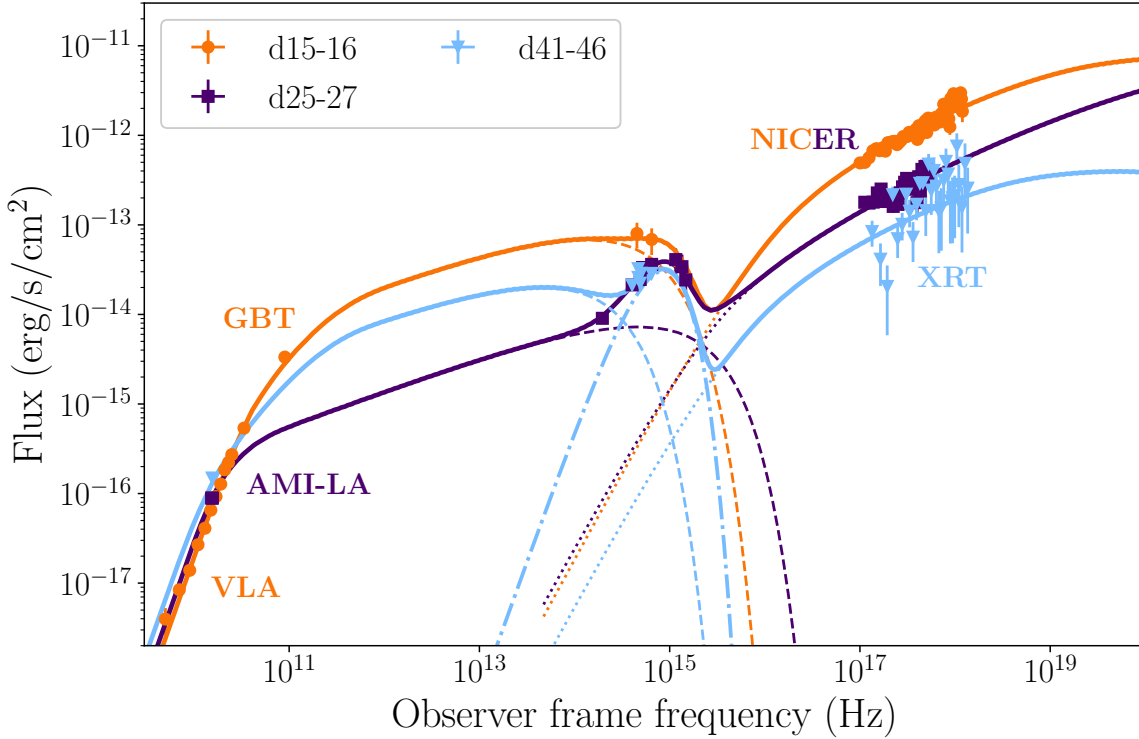


Figure 3: AT 2022cmc’s Multi-wavelength SEDs and their best-fit models. SEDs from three epochs (times given as days post discovery) are fitted with a single-zone jet model comprising synchrotron (dashed), synchrotron self-Compton (dotted), and black body (dash-dot) emission components. The radio data are consistent with optically-thick synchrotron emission, while the X-ray emission is well fit by SSC originating from the same emitting region. The strength of the SSC component implies a strongly matter-dominated jet, with $U_e/U_B \geq 10^2$. The optical data at 25-27 and 41-46 days after discovery exhibit an excess over the synchrotron+SSC model; as a result, we added a black body component of temperature $T_{bb} = 2.3 \times 10^4$ K (measured in the source frame) and luminosity $L_{bb} = 1.7 \times 10^{45}$ erg/s. The corresponding radius is $R_{bb} = 2.8 \times 10^{15}$ cm. Because of lack of optical/UV constraints on day 15-16, this component is assumed to remain constant between day 15-46 (see “Multi-wavelength SED modeling” and Extended Data Table 3 in Methods for more details). The data in this figure are available as a supplementary file.

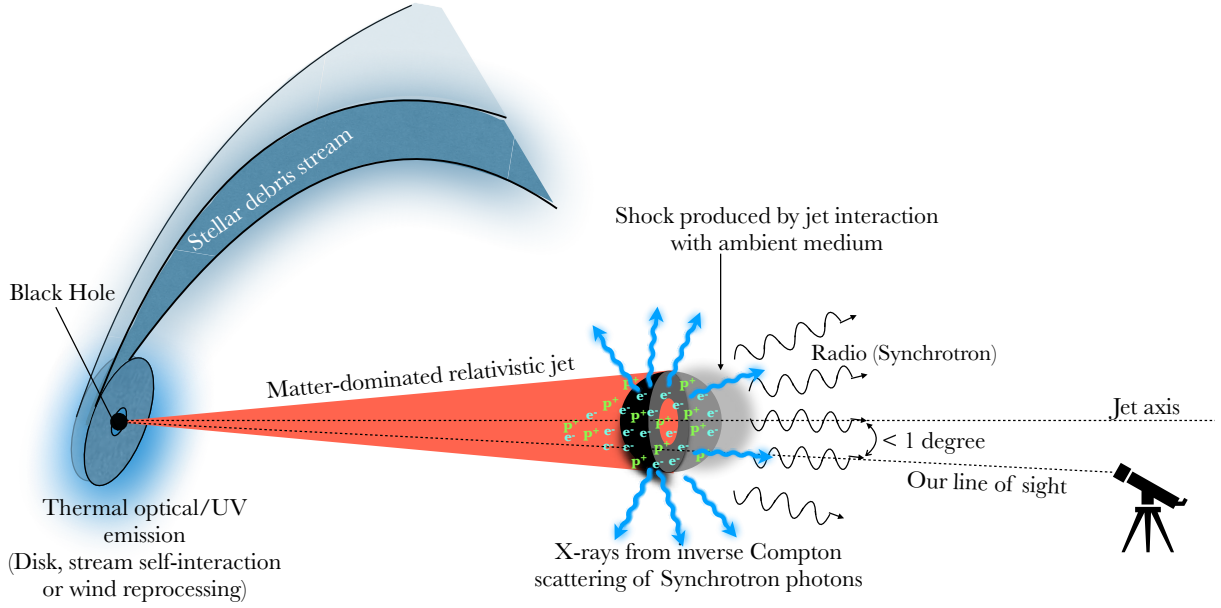


Figure 4: **Schematic of our proposed scenario for AT 2022cmc.** A mass-loaded, highly relativistic jet with a bulk Lorentz factor ~ 80 can explain AT 2022cmc’s multi-wavelength SED with radio emission originating from synchrotron processes and X-rays from SSC (see “Multi-wavelength SED modeling” and Extended Data Table 3 in Methods). The optical/UV emission part of the SED on day 25 is consistent with thermal emission with a temperature of $\sim 2.3 \times 10^4$ K and luminosity of 2×10^{45} erg s $^{-1}$ (rest-frame). These are comparable to low-z non-jetted TDEs (36). It could originate from an accretion disk, reprocessing by an outflow (e.g., (39)) or from stellar debris stream self-collisions (40). Our viewing angle with respect to the jet-axis is estimated from our SED modeling to be < 1 degrees (see Extended Data Table 3).

328 **Acknowledgments.**

329

330 SJB would like to thank their support from Science Foundation Ireland and the Royal Society
331 (RS-EA/3471).

332 S. Schulze acknowledges support from the G.R.E.A.T. research environment, funded by
333 *Vetenskapsrådet*, the Swedish Research Council, project number 2016-06012.

334 FO acknowledges support from MIUR, PRIN 2017 (grant 20179ZF5KS) "The new fron-
335 tier of the Multi-Messenger Astrophysics: follow-up of electromagnetic transient counter-
336 parts of gravitational wave sources" and the support of HORIZON2020: AHEAD2020 grant
337 agreement n.871158.

338 GL and PC were supported by a research grant (19054) from VILLUM FONDEN.

339 NCS acknowledge support by the Science and Technology Facilities Council (STFC), and
340 from STFC grant ST/M001326/.

341 MN, BG, AA, ER and XS are supported by the European Research Council (ERC) under
342 the European Union's Horizon 2020 research and innovation programme (grant agreement
343 No. 948381).

344 L. R. acknowledges the support given by the Science and Technology Facilities Council
345 through an STFC studentship.

346 TL acknowledges support from the Radboud Excellence Initiative.

347 TEMB acknowledges financial support from the Spanish Ministerio de Ciencia e Innovación
348 (MCIN), the Agencia Estatal de Investigación (AEI) 10.13039501100011033 under the
349 PID2020-115253GA-I00 HOSTFLOWS project, from Centro Superior de Investigaciones
350 Científicas (CSIC) under the PIE project 20215AT016 and the I-LINK 2021 LINKA20409,
351 and the program Unidad de Excelencia María de Maeztu CEX2020-001058-M.

352 CCN thanks for funding from the Ministry of Science and Technology (Taiwan) under the
353 contract 109-2112-M-008-014-MY3.

354 MPT acknowledges financial support from the State Agency for Research of the Spanish
355 MCIU through the "Center of Excellence Severo Ochoa" award to the Instituto de As-
356 trofísica de Andalucía (SEV-2017-0709) and through the grant PID2020-117404GB-C21
357 (MCI/AEI/FEDER, UE).

358 Support for AC was provided by ANID through grant ICN12_12009 awarded to the Mil-
359 lennium Institute of Astrophysics (MAS) and by ANID's Basal projects AFB-170002 and
360 FB210003.

361 Pan-STARRS is a project of the Institute for Astronomy of the University of Hawaii,
362 and is supported by the NASA SSO Near Earth Observation Program under grants
363 80NSSC18K0971, NNX14AM74G, NNX12AR65G, NNX13AQ47G, NNX08AR22G,
364 80NSSC21K1572 and by the State of Hawaii.

365 This publication has made use of data collected at Lulin Observatory, partly supported by
366 MoST grant 108-2112-M-008-001. We thank Lulin staff H.-Y. Hsiao, C.-S. Lin, W.-J. Hou
367 and J.-K. Guo for observations and data management.

368 This work was supported by the Australian government through the Australian Research
369 Council's Discovery Projects funding scheme (DP200102471).

370 The PanSTARRS1 Surveys (PS1) and the PS1 public science archive have been made possi-
371 ble through contributions by the Institute for Astronomy, the University of Hawaii, the Pan-
372 STARRS Project Office, the Max-Planck Society and its participating institutes, the Max
373 Planck Institute for Astronomy, Heidelberg and the Max Planck Institute for Extraterrestrial
374 Physics, Garching, The Johns Hopkins University, Durham University, the University of Ed-
375 inburgh, the Queen's University Belfast, the Harvard-Smithsonian Center for Astrophysics,
376 the Las Cumbres Observatory Global Telescope Network Incorporated, the National Central
377 University of Taiwan, the Space Telescope Science Institute, the National Aeronautics and
378 Space Administration under Grant No. NNX08AR22G issued through the Planetary Science
379 Division of the NASA Science Mission Directorate, the National Science Foundation Grant
380 No. AST-1238877, the University of Maryland, Eotvos Lorand University (ELTE), the Los
381 Alamos National Laboratory, and the Gordon and Betty Moore Foundation.

382 RR and DP acknowledge partial support from the NASA Grant, 80NSSC19K1287, for con-
383 tributions to NICER.

384 The European VLBI Network is a joint facility of independent European, African, Asian,
385 and North American radio astronomy institutes. Scientific results from data presented in this
386 publication are derived from EVN project code RM017A. e-VLBI research infrastructure in
387 Europe is supported by the European Union's Seventh Framework Programme (FP7/2007-
388 2013) under grant agreement number RI-261525 NEXPReS.

389 A.H. is grateful for the support by the I-Core Program of the Planning and Budgeting Com-
390 mittee and the Israel Science Foundation, and support by ISF grant 647/18. This research
391 was supported by Grant No. 2018154 from the United States-Israel Binational Science
392 Foundation (BSF). We acknowledge the staff who operate and run the AMI-LA telescope at
393 Lord's Bridge, Cambridge, for the AMI-LA radio data. AMI is supported by the Universities
394 of Cambridge and Oxford, and by the European Research Council under grant ERC-2012-
395 StG-307215 LODESTONE.

396 NICER is a 0.2-12 keV X-ray telescope operating on the International Space Station. The
397 NICER mission and portions of the NICER science team activities are funded by NASA.

398 The *AstroSat* mission is operated by the Indian Space Research Organisation (ISRO),
399 the data are archived at the Indian Space Science Data Centre (ISSDC). The SXT data-
400 processing software is provided by the Tata Institute of Fundamental Research (TIFR),
401 Mumbai, India. The UVIT data were checked and verified by the UVIT POC at IIA, Banga-
402 lore, India.

403 MG is supported by the EU Horizon 2020 research and innovation programme under grant
404 agreement No 101004719.

405 LJS acknowledges support by the European Research Council (ERC) under the European
406 Union's Horizon 2020 research and innovation program (ERC Advanced Grant KILONOVA
407 No. 885281).

408 MPT acknowledges financial support from the State Agency for Research of the Spanish
409 MCIU through the "Center of Excellence Severo Ochoa" award to the Instituto de As-
410 trofísica de Andalucía (SEV-2017-0709) and through the grant PID2020-117404GB-C21
411 (MCI/AEI/FEDER, UE).

412 Support for this work was provided by NASA through the Smithsonian Astrophysical Obser-
413 vatory (SAO) contract SV3-73016 to MIT for Support of the Chandra X-Ray Center (CXC)
414 and Science Instruments.

415 S. Y. has been supported by the research project grant "Understanding the Dynamic Uni-
416 verse" funded by the Knut and Alice Wallenberg Foundation under Dnr KAW 2018.0067,
417 and the G.R.E.A.T research environment, funded by *Vetenskapsrådet*, the Swedish Research
418 Council, project number 2016-06012.

419 SJS, SS, KWS, acknowledge funding from STFC Grant ST/T000198/1 and ST/S006109/1.

420 IA is a CIFAR Azrieli Global Scholar in the Gravity and the Extreme Universe Program
421 and acknowledges support from that program, from the European Research Council (ERC)
422 under the European Union's Horizon 2020 research and innovation program (grant agree-
423 ment number 852097), from the Israel Science Foundation (grant number 2752/19), from
424 the United States - Israel Binational Science Foundation (BSF), and from the Israeli Council
425 for Higher Education Alon Fellowship.

426 ECF is supported by NASA under award number 80GSFC21M0002.

427 The National Radio Astronomy Observatory is a facility of the National Science Foundation
428 operated under cooperative agreement by Associated Universities, Inc.

429 GPS acknowledges support from The Royal Society, the Leverhulme Trust, and the Science
430 and Technology Facilities Council (grant numbers ST/N021702/1 and ST/S006141/1).

431 L.G. acknowledges financial support from the Spanish Ministerio de Ciencia e Innovación
432 (MCIN), the Agencia Estatal de Investigación (AEI) 10.13039/501100011033, and the Eu-
433 ropean Social Fund (ESF) "Investing in your future" under the 2019 Ramón y Cajal program
434 RYC2019-027683-I and the PID2020-115253GA-I00 HOSTFLOWS project, from Centro
435 Superior de Investigaciones Científicas (CSIC) under the PIE project 20215AT016, and the
436 program Unidad de Excelencia María de Maeztu CEX2020-001058-M.

437 **Author contributions:** D.R.P led the overall project. **Competing interests:** The authors
438 declare that there are no competing interests. **Data and materials availability:** All the
439 *NICER* and *Swift* data presented here is public and can be found in the NASA archives at

440 the following URL: <https://heasarc.gsfc.nasa.gov/cgi-bin/W3Browse/w3browse.pl>. The multi-wavelength photometric values are provided as supplementary files. In addition, we also provide *NICER*, *Astrosat/SXT*, *Swift*, and long-GRB light curves used in Figure 1.

444 **Supplementary Materials.**

445 Materials and Methods

446 Extended Data Figures 1 to 8

447 Extended Data Tables 1 to 3

448 Supplementary Text

449

450 Methods.

451 1 Observations and Data Analysis

452 The data presented in this work was acquired by different telescopes/instruments across the
453 electromagnetic spectrum. Below, we describe the data and the relevant reduction and analysis
454 procedures. Throughout this paper, we adopt a standard Λ CDM cosmology with $H_0 = 67.4$
455 $\text{km s}^{-1} \text{Mpc}^{-1}$, $\Omega_m = 0.315$ and $\Omega_\Lambda = 1 - \Omega_m = 0.685$ (41).

456 1.1 γ -rays and X-rays

457 1.1.1 Fermi/LAT

458 AT 2022cmc was not detected by *Fermi*/Large Area Telescope (LAT; 100 MeV to 10 GeV).
459 During the 24 hour period starting on 27 February 2022 (UTC), i.e., days 15-16 after discovery,
460 the upper limits on the photon flux and the energy flux are 2.76×10^{-7} photons $\text{cm}^{-2} \text{s}^{-1}$, and
461 5.46×10^{-3} MeV $\text{cm}^{-2} \text{s}^{-1}$, respectively.

462 1.1.2 AstroSat/SXT

463 The *AstroSat* Soft X-ray Telescope (SXT; (42)) observed AT 2022cmc on 2022-02-23 for an
464 exposure time of 52.8 ks in the full window mode. We processed the level1 data using the
465 SXT pipeline *ASISXTLevel2-1.4b* available at the Payload Operation Center (POC) website [†],
466 and generated the orbit-wise cleaned event files which were then merged using the *SXTMerger*
467 tool[‡]. We extracted the source spectrum and light curve using a circular region of radius 15''
468 centered at the source position. We used the background spectrum and the redistribution matrix
469 files available at the POC. We used an updated ancillary response file. The 0.7 – 8 keV SXT
470 spectrum is consistent with a power law photon index of 1.8 ± 0.2 modified by absorption
471 column $N_H = (1.3 \pm 0.8) \times 10^{21} \text{ cm}^{-2}$ which is in excess of the Galactic column, $N_{\text{H,MW}} =$
472 $9 \times 10^{19} \text{ cm}^{-2}$. The observed flux is $5.1 \times 10^{-12} \text{ erg cm}^{-2} \text{s}^{-1}$ in the 0.7–8 keV band.

473 1.1.3 NICER

474 *NICER* started high-cadence monitoring (multiple visits per day) of AT 2022cmc on 2022-02-
475 16 19:07:03 (UTC) or MJD 59626.80, roughly 5 days after optical discovery. The resultant
476 dataset comprises of several hundred snapshots whose exposures varied between a few hundred
477 to roughly 1200 seconds. In this work, we report data taken prior to MJD 59697 (28 April
478 2022), i.e., from the first 76 days since discovery.

[†]https://www.tifr.res.in/~astrosat_sxt/sxtpipeline.html

[‡]<https://github.com/gulabd/SXTMerger.jl>

479 We started *NICER* data analysis by downloading the raw, unfiltered (*uf*) data from the
480 HEASARC public archive [§]. We reprocessed the data using the standard procedures outlined on
481 the *NICER* data analysis webpages (https://heasarc.gsfc.nasa.gov/docs/nicer/analysis_threads/). We follow the data reduction steps outlined in (43).

483 *NICER* is a non-imaging instrument with a field of view (FoV) of roughly 30 arcmin². To
484 test for the presence of potential contaminating sources in *NICER*'s field of view, we extract
485 a 0.3-8 keV X-ray image using *Swift*/XRT observations of the field (Extended Data Figure 1).
486 We find that AT 2022cmc is the only source within *NICER*'s FoV, implying that the flux from
487 AT 2022cmc dominates the *NICER* light curve at all times.

488 We investigate the X-ray spectral evolution of AT 2022cmc by extracting spectra from the
489 *NICER* data between MJD 59626 and 59642 at ≈ 0.5 day intervals (2). Spectral analysis from
490 data beyond MJD 59642, i.e., where AT 2022cmc's flux is reduced and comparable to the
491 *NICER* background, will be published in a separate work. We bin the spectra using the optimal
492 binning scheme described in (44), with the additional requirement that there be at least 25
493 counts per spectral bin. We implemented these using the `ftool ftgrouppha` with *groupype*
494 = *optmin* and *groupscale* = 25. We model these spectra in the 0.3-5.0 keV bandpass, the
495 energy range in which the source was above the background using a `tbabs` \times `ztbabs`
496 \times `zashift` (`clumin*power` law) model in *PyXspec*, a Python implementation[¶] of
497 *XSPEC* (45). We fix the Milky Way column to $N_{\text{H,MW}} = 9 \times 10^{19} \text{ cm}^{-2}$, estimated from
498 the HEASARC nH calculator[¶] (46). We tied the host galaxy neutral Hydrogen column to be
499 the same across all the spectra and incorporated an additional 1% systematic uncertainty while
500 fitting the data^{**}.

501 The above modeling resulted in a total χ^2 /degrees of freedom (dof) of 2135.3/1956. The
502 reduced χ^2 values are close to unity in all expect during epoch E21 in which systematic residuals
503 below 1 keV and above 5 keV are clearly present. This epoch coincides with a hard (2-5 keV)
504 X-ray flare. Multiple such flares are evident between MJD 59637 and 59697. One such flare is
505 also captured by *Swift* (see panel (d) of Figure 1). We defer the spectro-timing analysis of these
506 flares to a future work.

507 Following (47) we set *NICER*'s sensitivity limit to a conservative value of 0.3-5 keV count
508 rate of 0.2 counts/sec (normalized to 50 *NICER* detectors). In other words, any particular time
509 segment in which the background-subtracted 0.3-5 keV countrate is less than 0.2 cps is treated
510 as an upper limit of $7.4 \times 10^{45} \text{ erg s}^{-1}$. This upper limit corresponds to 0.3-10 keV absorption-
511 corrected luminosity of $1.2 \times 10^{46} \text{ erg s}^{-1}$ for a source at a redshift of 1.193 (see panel (a) of
512 Figure 1).

[§]<https://heasarc.gsfc.nasa.gov/cgi-bin/W3Browse/w3browse.pl>

[¶]<https://heasarc.gsfc.nasa.gov/xanadu/xspec/python/html/index.html>

[¶]<https://heasarc.gsfc.nasa.gov/cgi-bin/Tools/w3nh/w3nh.pl>

^{**}https://heasarc.gsfc.nasa.gov/docs/nicer/analysis_threads/cal-recommend/

513 **1.1.4 *Swift*/X-Ray Telescope(XRT)**

514 *Swift* was not operational during the optical detection of AT 2022cmc and the satellite resumed
515 pointed operations on 17 February 2022 (48). *Swift* began monitoring AT 2022cmc on MJD
516 59633 (23 February 2022). The source was observed once a day between MJD 59633 and
517 59638 and once every few days after MJD 59638. We started our data analysis by download-
518 ing the raw, level-1 data from the HEASARC public archive and reprocessed them using the
519 standard HEASoft tool `xrtpipeline`. Here, we only consider the data taken in the Photon
520 Counting (PC) mode. We only used events with graded between 0 and 12 in the energy range
521 of 0.3 and 5 keV to match *NICER*'s bandpass. We extracted the source and background counts
522 using a circular aperture of 47'' and an annulus with an inner and outer radii of 80'' and 200'',
523 respectively.

524 To convert *Swift*/XRT count rates to fluxes we extracted an average energy spectrum by
525 combining all the XRT exposures. We fit the 0.3-5.0 keV spectra with a power law model,
526 modified by AT 2022cmc's host galaxy neutral Hydrogen column and MilkyWay, same as the
527 model used for *NICER* data above. The host galaxy Hydrogen column was fixed at 9.8×10^{20}
528 cm^{-2} as derived from *NICER* fits. We left the power law photon index free which yielded
529 a best-fit value of 1.45 ± 0.06 . This value is consistent with *NICER* spectral fits. From this
530 fit we estimated the absorption-corrected flux and a count rate-to-flux scaling factor of $1.2 \times$
531 $10^{-10} \text{ erg cm}^{-2} \text{ counts}^{-1}$ to convert from 0.3-5 keV background-subtracted XRT count rate to
532 absorption-corrected flux (Figure 2).

533 **1.1.5 GRB and TDE Comparison Data**

534 In order to compare the X-ray light curve of AT 2022cmc with other relativistic transients, we
535 compile a sample of X-ray light curves of the three known relativistic TDEs, together with the
536 bright GRBs from (38). For the GRBs in our comparison sample, we download the 0.3–10 keV
537 count-rate light curves from the UK *Swift* Science Data Centre (UKSSDC) (49, 50) and correct
538 them for absorption using the ratio of time-averaged unabsorbed flux to time-averaged observed
539 flux per burst, provided in the UKSSDC catalog^{††}. We k-correct the light curves to rest-frame
540 0.3–10 keV luminosity following (51), assuming a power-law spectrum with photon index given
541 by the time-averaged photon-counting mode photon index from the UKSSDC catalog.

542 We extract X-ray light curves of the three relativistic TDEs using the UKSSDC XRT prod-
543 ucts builder^{‡‡} (49, 50). We use a time bin size of one day. We convert the 0.3–10 keV count
544 rate light curves to unabsorbed flux using the counts-to-flux ratio of the time-averaged spec-
545 tral fits, and k-correct them to rest frame 0.3–10 keV as described above. The relevant spectral
546 parameters are, Sw J644+57: cts:flux = $9.32 \times 10^{-11} \text{ erg cm}^{-2} \text{ ct}^{-1}$, photon index = $1.58 \pm$
547 0.01; Sw J1112.2-8238: cts:flux = $6.13 \times 10^{-11} \text{ erg cm}^{-2} \text{ ct}^{-1}$, photon index = 1.35 ± 0.08 ;
548 Sw J2058.4+0516: cts:flux = $5.36 \times 10^{-11} \text{ erg cm}^{-2} \text{ ct}^{-1}$, photon index = 1.55 ± 0.08 . We plot

^{††}https://www.swift.ac.uk/xrt_live_cat/

^{‡‡}https://www.swift.ac.uk/user_objects/

549 these light curves, together with the GRB X-ray light curves extracted above, in Figure 1.

550 1.2 UV/Optical Observations

551 1.2.1 Zwicky Transient Facility

552 AT 2022cmc was discovered and reported by the Zwicky Transient Facility (ZTF; (10)) and
553 released as a transient candidate ZTF22aaajecp in the public stream to brokers and the Transient
554 Name Server, with data available in Lasair⁵⁵ (52). We performed point spread function (PSF)
555 photometry on all publicly available ZTF data using the ZTF forced-photometry service (53) in
556 g - and r -band. We report our photometry, corrected for Galactic extinction of $A_V = 0.0348$ mag
557 (54) and converted to flux density in mJy, in Extended Data Table 1.

558 1.2.2 ATLAS

559 The Asteroid Terrestrial-impact Last Alert System (ATLAS; (55)) is a 4×0.5 meter telescope
560 system, providing all-sky nightly cadence at typical limiting magnitudes of ~ 19.5 in cyan ($g +$
561 r) and orange ($r + i$) filters. The data are processed in real time and the transients are identified
562 by the ATLAS Transient Science Server (56). We stacked individual nightly exposures and
563 used the ATLAS forced photometry server (57) to obtain the light curves of AT 2022cmc in
564 both filters. Photometry was produced with standard PSF fitting techniques on the difference
565 images and we initially reported the fast declining optical flux in (11).

566 1.2.3 Follow-up optical imaging

567 Followup of AT 2022cmc was conducted as part of the “advanced” extended Public ESO Spec-
568 troscopic Survey of Transient Objects (ePESSTO+) (58) using the EFOSC2 imaging spectro-
569 graph at the ESO New Technology Telescope to obtain images in g , r and i bands. Images
570 were reduced using the custom PESSTO pipeline (<https://github.com/svalenti/pessto>), and the PSF photometry was measured without template subtraction using *photometry-
571 sans-frustration*; an interactive python wrapper utilising the Astropy and Photutils packages
572 (59). Aperture photometry was applied to the few images in which the target PSF was slightly
573 elongated, otherwise the magnitudes were derived from PSF-fitting. All photometry has been
574 calibrated against Pan-STARRS field stars.

576 AT 2022cmc was also followed up in r , i , z and w bands with the 1.8 meter PanSTARRS2
577 (PS2) telescope in Hawaii (60). PS2 operates in survey mode, searching for near-Earth objects
578 but the survey can be interrupted for photometry of specific targets. PS2 is equipped with a
579 1.4 Gigapixel camera with a pixel scale of $0.26''$. The images were processed with the Image
580 Processing Pipeline (IPP; (61)) and difference imaging was performed using the PS1 Science

⁵⁵<https://lasair.roe.ac.uk/object/ZTF22aaajecp>

581 Consortium (PS1SC; (60)) 3π survey data as reference. PSF photometry was used to compute
582 instrumental magnitudes, and zero-points were calculated from PS1 reference stars in the field.

583 AT 2022cmc was also observed as part of the Kinder (kilonova finder) survey (62) in g ,
584 r , and i bands with the 0.4m-SLT at Lulin Observatory, Taiwan. The images were reduced
585 using a standard IRAF routine with bias, dark and flat calibrations. We used the AUTOnomous
586 Photometry Of Transients (AutoPhOT) pipeline (63) to perform PSF photometry and calibrate
587 against SDSS field stars (64). We used the Lulin one-meter telescope (LOT) for deeper imaging
588 in g , r , i and z bands over four nights spanning 13.4–16.2 days after discovery. The images were
589 also reduced using the standard CCD processing techniques in IRAF. We performed aperture
590 photometry calibrated against SDSS field stars. In a combined stack of the images from the
591 LOT, AT 2022cmc was clearly detected in g , r and i bands, with magnitudes 21.76 ± 0.14 ,
592 21.71 ± 0.18 and 21.93 ± 0.31 mag, respectively and undetected in z band with an upper limit
593 of > 20.69 mag. We list the photometry from our individual observations in the Extended Data
594 Table 1.

595 We compile additional optical photometry from the GCN circulars (65–75) and correct for
596 extinction. These are also included in the Extended Data Table 1.

597 1.2.4 *Swift*/UVOT

598 We perform photometry on *Swift*/UVOT (76) observations of AT 2022cmc with the *uvotsource*
599 task in HEAsoft package v6.29 using a 5" aperture on the source position. Another region of
600 40" located at a nearby position was used to estimate the background emission. Because the
601 host galaxy is not detected in the GALEX (77) coadded UV images and AT 2022cmc's UVOT
602 detections are ~ 2 mag brighter than host upper limits (see “Constraints on host luminosity”),
603 we did not attempt any type of host subtraction.

604 1.2.5 *AstroSat*/UVIT

605 The *AstroSat* Ultra-Violet Imaging Telescope (UVIT (78, 79)) onboard *AstroSat* (80) also ob-
606 served the source, simultaneous with the SXT, with its Far Ultra-violet (FUV) channel using
607 the F148W ($\lambda_{mean} = 1481\text{\AA}$; $\Delta\lambda = 500\text{\AA}$) and F154W ($\lambda_{mean} = 1541\text{\AA}$; $\Delta\lambda = 380\text{\AA}$) fil-
608 ters for exposures of 6024s and 9674s, respectively. We processed the level1 data using the
609 CCDLAB pipeline (81) and constructed broadband images. We extracted source counts using
610 a circular aperture of radius 10" centered at the source position. We also extracted background
611 counts from nearby source-free regions, and corrected for the background contribution. We
612 then converted the net count rates to the flux densities using the flux conversion factors pro-
613 vided in (78, 79). We do not detect the source, and obtain 3σ flux upper limits of 4.7×10^{-17}
614 $\text{erg cm}^{-2} \text{s}^{-1} \text{\AA}^{-1}$ (F154W) and $6.4 \times 10^{-17} \text{erg cm}^{-2} \text{s}^{-1} \text{\AA}^{-1}$ (F148W).

615 **1.2.6 Optical spectroscopy**

616 We observed AT 2022cmc with the X-shooter spectrograph (82) on the European Southern
617 Observatory's Very Large Telescope (VLT) on 27 February 2022. Data were obtained in on-slit
618 nodding mode using the 1.0'', 0.9'', and 0.9'' slits in the UVB, VIS and NIR arms respectively,
619 with a spectral resolution of $\approx 1 \text{ \AA}$ in the optical. We reduced the data following standard
620 procedures (83). We first removed cosmic-rays with the tool `astroscrappy`[¶], which is
621 based on cosmic-ray removal algorithm by (84). Afterwards, we processed the data with the
622 X-shooter pipeline v3.3.5 and the ESO workflow engine ESOREflex (85, 86). We reduced the
623 UVB and VIS-arm data in stare mode to boost the SN by a factor of $\sqrt{2}$ compared to the
624 standard nodding mode reduction. We co-added the individual rectified and wavelength- and
625 flux-calibrated two-dimensional spectra, followed by extraction of the one-dimensional spectra
626 of the each arm in an statistically optimal way using tools developed by J. Selsing***.Finally,
627 we converted the wavelength calibration of all spectra to vacuum wavelengths and corrected
628 the wavelength scale for barycentric motion. We stitched the spectra from the UVB and VIS
629 arms by averaging in the overlap regions. We reduced the NIR data reduced in nodding mode
630 to ensure a good sky-line subtraction. We do not detect a trace of the target in the NIR arm and
631 thus do not discuss the NIR data further.

632 The extracted spectrum consists of a steep and largely featureless blue continuum, which
633 we rebin by 5 pixels to increase the S/N (Extended Data Figure 3). At the reported redshift $z =$
634 1.193, there is a hint of absorption features at wavelengths consistent with the Ca II H&K lines.
635 The apparent absorption at $\sim 2600 \text{ \AA}$ is not a real feature, but rather a low-sensitivity, noisy
636 region close to the edge of the UVB arm. The spectrum (covering rest-frame $\sim 1500 - 4500 \text{ \AA}$)
637 can be well fit by a blackbody with $T \approx 30,000 \text{ K}$, though a power law with $F_\nu \propto \nu^{0.6}$ also
638 provides a satisfactory fit. The thermal model is preferred due to its consistency with the optical
639 bump in the broad-band SED (Figure 3). This value is consistent with the measurement of
640 $\sim 2.3 \times 10^4 \text{ K}$ from the optical/UV SED, after accounting for the synchrotron contribution and
641 the measurement uncertainty of $\sim 10\%$ on the value inferred from the VLT spectrum. This
642 inferred temperature is similar to other optical TDEs (87).

643 **1.2.7 Constraints on host luminosity**

644 In order to put upper limits on the luminosity of the host galaxy, we created deep reference im-
645 ages in w, i, z bands by stacking PanSTARRS1 and PanSTARRS2 images of the field containing
646 AT 2022cmc. These images were obtained during routine survey operations over a period span-
647 ning June 2010 to January 2022. The w -band is a wide filter ($3900 - 8500 \text{ \AA}$) with an effective
648 wavelength $\lambda_{\text{eff}} \approx 6000 \text{ \AA}$, and can thus be treated as r -band. The effective exposure time for
649 the co-added reference stacks is 2475 s, 13700 s, 16260 s, in w, i, z bands respectively. The
650 host galaxy of AT 2022cmc is not visible in any of these stacks, with upper limits of $w > 23.85$,

[¶]<https://github.com/astropy/astroscrappy>

***https://github.com/jselsing/XSGRB_reduction_scripts

651 $i > 23.05$ and $z > 22.89$ mag (see Extended Data Figure 5).

652 The deepest observer-frame limit (r -band) corresponds to rest-frame absolute AB magni-
653 tude of $M_{2740} > -19.9$, with a simple k -correction of $2.5 \log(1 + z)$ and the observer frame
654 central wavelength converted to rest-frame (approximately 2740Å), with only a Milky Way red-
655 dening correction applied to the observer frame flux. The redder bands similarly correspond to
656 $M_{3430} > -20.7$ and $M_{3950} > -20.8$. We performed a similar analyses on GALEX (77) *NUV*
657 ($\lambda_{\text{eff}} \approx 2300$ Å) and *FUV* ($\lambda_{\text{eff}} \approx 1535$ Å) filters data by stacking all images that contains the
658 position of AT 2022cmc. No underlying host emission is detected in any of stacked images, and
659 the 3σ upper limits are *NUV* > 22.6 and *FUV* > 22.5 mag.

660 1.3 Radio

661 1.3.1 VLA

662 We observed AT 2022cmc on 2022 February 27 (≈ 15 d after discovery) with NSF's Karl G.
663 Jansky Very Large Array (VLA) under program 20B-377 (PI: Alexander). The observations
664 were taken when the array was in its most extended A configuration. We used the C, X, Ku,
665 K, and Ka band receivers with the 3-bit digital samplers to obtain nearly continuous frequency
666 coverage from 4 – 37 GHz. We used 3C286 for bandpass and flux density calibration. We
667 used J1329+3154 for complex gain calibration at K and Ka bands, and 3C286 otherwise. We
668 reduced and imaged the data using standard procedures in the Common Astronomy Software
669 Applications (CASA) v5.6.1-8 (88). We detect a bright unresolved point source at all frequen-
670 cies, enabling us to split the data into 2 GHz bandwidth segments for photometry. The resulting
671 SED is shown in Figure 3.

672 1.3.2 Arcminute Microkelvin Imager - Large Array

673 The Arcminute Microkelvin Imager – Large Array (AMI-LA) is a radio interferometer con-
674 sisting of eight 12.8 metre dishes with baselines from 18 to 110 metres, located in Cambridge,
675 UK (89). AMI-LA observes at 15.5 GHz with a bandwidth of 5 GHz divided into 4096 chan-
676 nels (90). We observed AT 2022cmc with AMI-LA beginning 14.7 days after discovery (7).
677 We reduced the AMI-LA observations using a custom pipeline REDUCE_DC (91). The pipeline
678 averages the data down to 8 channels, performs flagging for radio frequency interference and
679 antenna shadowing. We used 3C286 for both amplitude and complex gain calibration. We per-
680 formed additional flagging, imaging and deconvolution in CASA (Version 4.7.0). We combine
681 the statistical uncertainty on the 15.5 GHz flux densities with a 5% systematic calibration uncer-
682 tainty in quadrature. We detected an unresolved source with a flux density of 0.49 ± 0.03 mJy in
683 the first epoch (92), and initiated subsequent observations at near-daily cadence. We present the
684 full 15.5 GHz light curve in Figure 2 and list the flux density measurements in Extended Data
685 Table 1. We compile additional radio measurements of AT 2022cmc reported online in GCN
686 circulars and Astronomer's Telegrams (65, 93, 94) together in Extended Data Table 1.

687 **1.3.3 EVN sub-milliarcsecond position**

688 We used the European Very Long Baseline Interferometry (VLBI) Network (EVN) to observe
689 AT 2022cmc on 2022 March 22–23 (18:08–02:11 UTC), under project code RM017A (PI:
690 Miller-Jones), making use of the real-time eVLBI mode. We observed in dual-polarization
691 mode, at a central frequency of 4.927 GHz. Our array consisted of 15 stations, with ten stan-
692 dard EVN stations (Jodrell Bank Mk II, Effelsberg, Hartebeesthoek, the 16-m dish at Irbene,
693 Medicina, Noto, the 85' dish at Onsala, the 65-m dish at Tianma, Torun, and Yebes) that ob-
694 served with a bandwidth of 256 MHz, and five stations from the eMERLIN array (Knockin,
695 Darnhall, Pickmere, Defford, and Cambridge), which observed with a reduced bandwidth of
696 64 MHz.

697 We processed the data through the EVN pipeline to derive the a priori amplitude calibration
698 and bandpass corrections, and conducted further processing with the Astronomical Image Pro-
699 cessing System (AIPS, version 31DEC19 (95)). We phase referenced the data on AT 2022cmc
700 to the nearby (1.66° away) calibrator source J1329+3154, with an assumed position of (J2000)
701 13:29:52.864912, +31:54:11.05446. We detected AT 2022cmc as an unresolved point source
702 with a significance of 6.4σ , at a position of (J2000) 13:34:43.201308(6), +33:13:00.6506(2).
703 The quoted uncertainties (denoted in parentheses for the last significant digit) are purely statis-
704 tical, with potential systematic errors (e.g. from uncorrected tropospheric delay or clock errors)
705 estimated to be at the level of ~ 0.07 mas.

706 **2 Shortest X-ray variability timescale**

707 Manual inspection of the 0.3–5 keV background-subtracted *NICER* light curve of AT 2022cmc
708 (provided as a supplementary file) reveals multiple instances of a variation in the observed count
709 rate by $> 50\%$ within a span of a few hundred seconds. To quantify the variability timescale,
710 we extracted an average power density spectrum (PDS) using uninterrupted exposures that were
711 each 950 s long^{†††} within the first month of discovery, i.e., data acquired before MJD 59642
712 (rapid flaring activity observed at later times will be considered in a separate work). To ensure
713 minimal impact from background fluctuations, we only considered exposures that were above
714 the background, i.e., background-subtracted 0.3–5 keV count rates greater than 0.2 counts/s
715 (normalized to 50 *NICER* detectors), close to the nominal limit described by (47). In addition
716 to the standard filters described in “ γ -ray and X-rays/*NICER*” we impose a filter to remove
717 exposures where the observed mean 15–18 keV count rate is beyond two standard deviations
718 of the median 15–18 keV rate measured across all exposures. This is an extra-cautious step
719 to minimize the effect of background particle flaring which is important for variability studies.
720 This gives a total of 29 time series with a cumulative exposure of 27.55 ks (950×29). We
721 compute a Leahy-normalized ((96); mean Poisson noise level of 2) average power density

^{†††}Increasing the accumulation time to 1024 s exposures yields fewer samples (13, compared to 29) and only results in a marginal gain in low frequency information from 1/950 Hz to 1/1024 Hz.

722 spectrum (PDS) sampled at 1/8 seconds from these time series (Extended Data Figure 4). We
723 find that the PDS is consistent with the Poisson noise level of 2 at high frequencies ($\gtrsim 10^{-2}$ Hz);
724 however, the PDS starts to rise above the noise level at $\lesssim 2 \times 10^{-3}$ Hz, and the lowest-frequency
725 bin at 1/950 s clearly well-above the noise level. This suggests that AT 2022cmc has systematic
726 X-ray variability on timescales at least as short as ~ 1000 s in observer frame.

727 **3 Arguments against a GRB afterglow**

728 A potential association with the *Fermi* Gamma Ray Burst (GRB) 220211A (97) was ruled out
729 following a more precise localization of that GRB (98). Nevertheless, the early optical evo-
730 lution resembled an off-axis gamma-ray burst (GRB). Long GRBs occur as a result of the
731 core-collapse of massive stars (e.g., (99–101)). Their emission comes in two phases: prompt
732 emission, which consists of high-energy γ -rays generated within the ultra-relativistic jet that is
733 launched following collapse (102, 103), and the afterglow, which is produced by shocks as the
734 jet is decelerated in the environment surrounding the burst (104, 105). High-cadence *NICER*
735 and *Swift/XRT* monitoring observations have shown that AT 2022cmc has been consistently
736 brighter than even the most luminous known GRB afterglows by more than a factor of 10 (see
737 panel (a) of Figure 1). The most striking difference between AT 2022cmc and GRB afterglows
738 is the persistence of rapid X-ray variability (e.g., Figure 1 panels (a)–(d), and see Extended Data
739 Figure 4). The *NICER* observations reveal short (≈ 2.4 hrs observer frame, corresponding to
740 ≈ 1 hr in the source rest frame) flares with increases in the count rate by factors of 2–10 that
741 remain detectable until at least ≈ 40 days after discovery. This variability requires that the X-
742 ray emitting region be smaller than $R = 2\Gamma_j^2 c\delta t \approx 10^{-4} \Gamma_j^2$ parsec (where Γ_j is the bulk Lorentz
743 factor of the jet). In contrast, the expected tangential radius of a GRB afterglow at a similar time
744 is ≈ 0.5 pc for typical parameters (106) and $\Gamma_j \lesssim 2$. Continued central engine activity, which
745 operates at much smaller radii ($\sim 10^{13}$ cm, e.g. (107)) may produce rapid variability (108),
746 but even the longest GRBs (the so-called ‘ultra-long’ class; (109)) do not show signs of central
747 engine activity beyond a day after trigger (e.g. (110)). On the other hand, X-ray variability on
748 timescales of tens of minutes has been inferred for the relativistic TDEs, Sw J1644+57 (111)
749 and Sw J2058+05 (112). These properties strongly favour a non-GRB origin.

750 **4 Multi-wavelength SED modeling**

751 **4.1 Preliminary Considerations**

752 The full multi-wavelength (radio to X-ray) spectral energy distribution of AT 2022cmc can-
753 not be simply explained by synchrotron emission. To see this, we consider the SED at \approx
754 15.6 days after discovery (Extended Data Figure 6) at radio (VLA), mm-band (GBT), ultravi-
755 olet (*Swift/UVOT*) and X-ray frequencies (*NICER*). We find that the spectral index from the
756 GBT mm-band (90 GHz) observation to the center of the *NICER* X-ray band is approximately

757 $\beta_{\text{mm-X}} \approx -0.63$ (corresponding to $\nu F_\nu \propto \nu^{0.37}$). This is inconsistent with the observed hard
 758 NICER spectrum, $\beta_X \approx -0.43$ (corresponding to $\nu F_\nu \propto \nu^{0.57}$). Furthermore, the interpolation
 759 from the radio to the X-rays using the above spectral index over-predicts contemporaneous
 760 *Swift/UVOT UM2*-band observations (when corrected for Galactic extinction) by a factor of
 761 ≈ 4 . While extinction due to dust could suppress the UV flux, there is no evidence for signifi-
 762 cant dust extinction along the line of sight, as evidenced by the blue $z' - g' \approx -0.1$ mag colour
 763 as well as the blue optical spectrum at this time (Section 1.2.6). The absence of significant
 764 extinction is further confirmed by the *HST F160W* and *F606W* measurements at ≈ 25.4 days,
 765 which yield a spectral index of $\beta_{F606-F160} = 0.34 \pm 0.08$. Thus, it is not possible to extend
 766 a single power-law spectrum from the radio to the X-rays without a mismatch between the re-
 767 quired spectral index and the observed X-ray spectral index, and without over-predicting the
 768 optical/UV flux, indicating that the radio and X-ray flux arise from distinct emission compo-
 769 nents at this time.

770 Furthermore, the optical SED at this time appears to peak in $\approx g$ -band, with a spectral index
 771 $\beta_{g-\text{um2}} = -1.5 \pm 0.5$. This declining spectral index cannot connect with observed X-ray flux,
 772 as the spectral index between the optical and X-rays at this time is much harder, $\beta_{\text{opt-X}} \approx -0.2$.
 773 This suggests that the optical and X-ray emission at this time also arises from separate emission
 774 components. This is further confirmed by the very different temporal evolution in the X-rays
 775 ($\alpha_X \approx -2.2$ and optical ($\alpha_r \approx -0.3$) at ≈ 10 –40 days post-discovery).

776 The radio SED at $\lesssim 25$ GHz is optically thick ($\beta \approx 2$), whereas the spectral index between
 777 the flux density measured with the VLA 24.5 GHz and with the GBT at 90 GHz is $\beta_{\text{K-mm}} =$
 778 -0.96 ± 0.06 , indicating a spectral break is present near the GBT frequency. A simple broken
 779 power-law fit to the radio-mm SED at this time with the post-break index fixed at $\beta \approx -1$
 780 yields a break frequency of $\nu_{\text{pk}} = (57.5 \pm 0.1)$ GHz and a spectral peak flux density of $F_{\nu,\text{pk}} =$
 781 (4.1 ± 0.1) mJy at 15.6 days. Identifying this as the peak of a synchrotron SED, a simple energy
 782 equipartition argument suggests a minimum kinetic energy of $E_{\text{K,iso}} \approx 10^{50}$ erg and radius
 783 of $R_{\text{eq}} \approx 10^{16}$ cm for this component (113). In the next section, we relax the assumption of
 784 equipartition and perform a full model fit with a physical model including SSC emission in the
 785 X-rays and a black body component in the optical.

786 4.2 Model setup

787 For our model fits, we create three SEDs of AT 2022cmc by combining the data taken on days
 788 15–17, 25–27, and 41–46, as these epochs have the best multi-wavelength coverage. We fit
 789 each SED with a simple homogeneous single zone model, similar to those used for blazars,
 790 e.g. (8, 25, 26). In this model, a power-law energy distribution of electrons with number density
 791 n_e , energy index p , and minimum and maximum Lorentz factors γ_{min} and γ_{max} , is injected
 792 in a spherical region of radius R , threaded with a magnetic field B and moving with a bulk
 793 Lorentz factor, Γ_j with respect to the observer at viewing angle, θ . The quantities B , n_e and
 794 R are calculated in the emitting region co-moving frame. We test two different model setups
 795 in order to probe which radiative mechanisms are responsible for the high energy emission. In

796 the simplest case (which we call model 1), we consider synchrotron and SSC exclusively. In
797 the second case, we test a simple external inverse Compton model (model 2 from now on), in
798 which the seed photons are provided by the optical black body component ^{***}.

799 Modelling the UV/optical emission as, e.g., a disk wind is very complex and beyond the
800 scope of this work (34). Given the thermal appearance of the UV/optical SED, we make the
801 simplifying assumption that this is black body emission originating in a thin shell at a radius
802 $R_{\text{bb}} = (L_{\text{bb}}/4\pi\sigma_{\text{sb}}T_{\text{bb}}^4)^{1/2}$ (in analogy with how blazar jet models typically treat the torus
803 around the AGN, e.g. (25)), and derive L_{bb} and T_{bb} from the temperature and normalization
804 of the thermal component as we run the fit. In order to estimate the relative contribution of
805 EC and SSC we need to calculate the energy density in the co-moving frame of the jet. For
806 this, we need to assume an opening angle ϕ to convert the radius of emitting region R to a
807 distance from the central engine. For simplicity, we take $\phi = 1/\Gamma_j$ and estimate the distance
808 from the black hole to be $d = R/\phi = \Gamma_j R$. Finally, we calculate the black body energy
809 density U_{bb} as follows. For $d < R_{\text{bb}}$, the emitting region in the jet is moving towards the
810 black body (in which case EC is expected to contribute meaningfully to the SED) and we have
811 simply $U_{\text{bb}} = \Gamma_j^2 L_{\text{bb}}/(4\pi R_{\text{bb}}^2 c)$. For $d \geq R_{\text{bb}}$, we account self consistently (following the
812 prescription in (115) for an AGN torus) for the de-boosting of the photons, as the jet emitting
813 region is moving away, rather than towards, the optical-emitting region. This choice of jet
814 opening angle means that the efficiency of EC is maximized with respect to SSC. This is because
815 maximizing the jet opening angle (by setting $\phi = 1/\Gamma_j$) minimizes the distance d from the black
816 hole for a given radius R , which in turn makes it more likely that the optical photons will be
817 Doppler-boosted in the frame of the jet. We note that for AGN jets, VLBI surveys find typical
818 values of $\phi \approx 0.1 - 0.2\Gamma_j$ (116). This smaller opening angle would push the emitting region
819 farther away from the black body, reducing the efficiency of EC. The cyclo-synchrotron and
820 inverse Compton emission are calculated using the Kariba libraries from the BHJet publicly
821 available model (115).

822 We import the data and model into the spectral fitting package **ISIS**, version 1.6.2-51 (117)
823 and jointly fit the SEDs at the three epochs. We tie the minimum Lorentz factor γ_{min} , the
824 particle distribution slope p , the bulk Lorentz factor Γ_j and the viewing angle θ across all epochs
825 (meaning the parameters are free during the fit, but forced to be identical for each SED) and
826 jointly fit all three SEDs, aiming to simplify the parameter space as much as possible. To obtain
827 a starting guess for the model parameters, we perform an uncertainty-weighted least-squares fit
828 using the χ^2 statistic with the `subplex` minimization algorithm. We then explore the parameter
829 space via Markov Chain Monte Carlo (MCMC) with `emcee` (118) using 50 walkers for each
830 free parameter (for a total of 900 walkers). We run the MCMC for 15000 steps and discard the
831 first 6000 as “burn-in”. We report the median and 1σ credible intervals (corresponding to 68%
832 of the probability mass around the median) on each parameter, as well as additional derived
833 quantities of interest, in Extended Data Table 3. We present the model corresponding to the
834 median values of the parameters in Figures 3 and Extended Data Figure 8 for models 1 and

^{***}Unlike (114), we can not test whether the seed photons originate in the accretion disk, as this component is not detected in any of the SEDs we model and is therefore entirely unconstrained.

835 2, respectively. We also show the 2d posterior distributions of the best-fitting parameters (for
836 model 1) that exhibit some degeneracy in Extended Data Figure 7.

837 4.3 Modelling results

838 In the case of model 1, we find that all the model parameters are well constrained by the data
839 with minimal degeneracy, as is typical of single-zone models (e.g. (27, 119)). The constraints
840 are weaker for model 2, but the model parameters remain fairly well determined. This behaviour
841 can be understood as follows. The SED samples 7 observable quantities: the synchrotron self-
842 absorption frequency ν_t (set by the multiple radio points on the day 15-16 SED), the synchrotron
843 luminosities in the optically thin and thick regimes $L_{s,\text{thin}}$ and $L_{s,\text{thick}}$ (constrained by the radio
844 and optical data), the inverse Compton luminosity L_{ssc} (set by the NICER data), the X-ray
845 photon index, the synchrotron scale frequency ν_s , and the inverse Compton scale frequency ν_c .
846 The free parameters in the model affect each observable quantity differently, and as a result it is
847 possible to relate one to the other. For example, the bolometric synchrotron luminosity scales as
848 $L_s \propto n_e R^3 B^2 \delta^4$, while the SSC bolometric luminosity scales as $L_{\text{ssc}} \propto n_e R^3 \delta^4 U_s$, with $U_s =$
849 $L_s / 4\pi R^2 c \delta^4$. As a result, $L_{\text{ssc}} \propto n_e^2 B^2 R^4 \delta^4$, so that $L_{\text{ssc}}/L_s \propto n_e R$: for a fixed synchrotron
850 luminosity, the large X-ray luminosity observed with *NICER* requires a large number density
851 and/or a large emitting region. In similar fashion, B , n_e , R and δ are further constrained by the
852 dependency of ν_t , $L_{s,\text{thick}}$, ν_s and ν_c on the model parameters. The constraints on the remaining
853 model parameters are more intuitive. The slope of the electron distribution p is determined by
854 the slope of the X-ray spectra, because (to first order) a power-law electron distribution produces
855 a power-law SSC spectrum with spectral index, $\beta = (1 - p)/2$. Finally, once B and δ are
856 determined, the minimum and maximum particle Lorentz factors γ_{\min} and γ_{\max} are constrained
857 by requiring that the synchrotron spectrum fall between the radio and optical frequency, and
858 that the low energy end of the SSC spectrum fall between UV and X-ray energies.

859 The main results of model 1 are as follows. First, we require the jet to be highly relativistic
860 ($\Gamma_j = 86_{-9}^{+10}$), viewed at a very small angle ($\theta \leq 1^\circ$) and very powerful ($\approx 10^{46-47} \text{ ergs}^{-1}$,
861 depending on the epoch and jet matter content). For comparison, this power is near or at the
862 Eddington luminosity of a $10^8 M_\odot$ black hole (roughly the largest black hole mass for which a
863 main sequence star can be tidally disrupted). Second, the size of the emitting region is $\approx 10^{15} -$
864 10^{16} cm , which is marginally consistent with the observed variability time-scale of $\approx 1000 \text{ s}$,
865 thanks to the strong beaming ($\delta \approx 100$). Finally, all of our best-fitting models require the
866 energy density of the electrons ($U_e = \langle \gamma \rangle n_e m_e c^2$, where $\langle \gamma \rangle$ is the average Lorentz factor of
867 the radiating electrons) to be larger than that of the magnetic field ($U_b = B^2/8\pi$) by a factor
868 $\approx 10^2$ (up to 10^5 for days 25-27, although this number is likely driven by our choice of tying
869 multiple parameters), implying that the bulk of the jet power is carried by the matter, rather than
870 the magnetic field.

871 The picture is quite different in the case of model 2. First, this model requires a small
872 emitting region radius ($R \approx 10^{14} \text{ cm}$) and jet Lorentz factor ($\Gamma_j \approx 5$). This behavior occurs
873 because if EC is to contribute meaningfully to the SED, the emission has to originate close

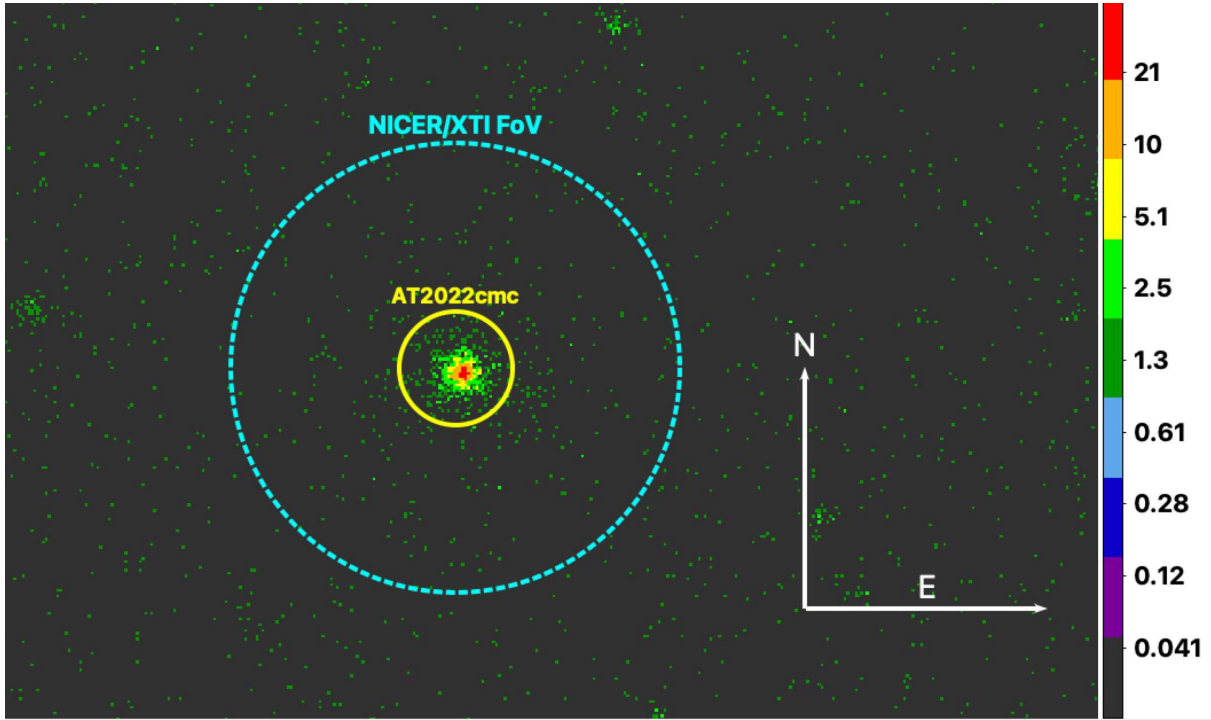
enough to the black hole that $d \leq R_{\text{bb}}$, so that the external photons are Doppler boosted in the jet co-moving frame. Invoking a smaller emitting region results in larger estimates for the magnetic field B and electron number density n_e . In turn, this causes the synchrotron self absorption frequency to move to $\approx 10^{12}$ Hz, well above where the observed break lies in the data, and suppressing the predicted radio flux as a result. Consequently, the EC model predicts negligible radio flux, and the radio emission in this model must originate in a separate region. Requiring not one but two individual, self-absorbing active regions in the jet means that this EC model would require significantly more fine-tuning than the SSC model. We account for the inability of the EC model to reproduce the observed radio flux by neglecting the radio data entirely in the final model 2 fits (not doing so causes the fit to either recover the model 1 fits, or produce fits with $\chi^2/\text{d.o.f} \approx 70$, rather than ≈ 2.3 without the radio data). Neglecting the constraints provided by the self-absorbed synchrotron data also means that the best-fitting parameters for model 2 are less well determined. Additionally, for seed black body photons peaking at $\nu_{\text{bb}} \approx 10^{15}$ Hz, the EC component only begins to be important at a frequency $\nu_{\text{EC}} \approx \delta\Gamma_j \gamma_{\text{min}}^2 \nu_{\text{bb}} \approx 10^{18}$ Hz (27). This scaling causes the EC component to only produce bright hard X-ray and/or soft γ -ray emission, while under-predicting the soft X-ray flux. Instead, at frequencies $\leq 10^{18}$ Hz the bulk of the flux is still produced through SSC, as in model 1. A similar behavior is also found when modelling the SEDs of powerful blazars (25, 26, 29), in which the X-ray emission typically originates through SSC, while the γ -ray emission is dominated by EC. Similarly to model 1, producing a large soft X-ray flux through SSC requires the jet to again be matter dominated, with $U_e/U_b \approx 100$. Finally, model 2 requires smaller jet powers, with $P_j \approx 10^{45}$ erg s $^{-1}$.

In summary, model 1 can satisfactorily fit the data at every epoch, although requiring a very highly beamed, matter-dominated jet. Model 2 on the other hand greatly under-predicts the radio data, which instead requires some fine-tuning in the form of a second self-absorbed emitting region further downstream. While in this case the beaming requirements are less severe, a large SSC contribution is still required to match the X-ray flux, resulting in a similarly matter-dominated jet to model 1. Due to all these considerations, we favour model 1 over model 2, with the caveat that our treatment of the EC process is fairly simplistic. Despite this caveat, the models presented here provide strong evidence that the emission of AT 2022cmc originates in a relativistic jet pointed towards Earth.

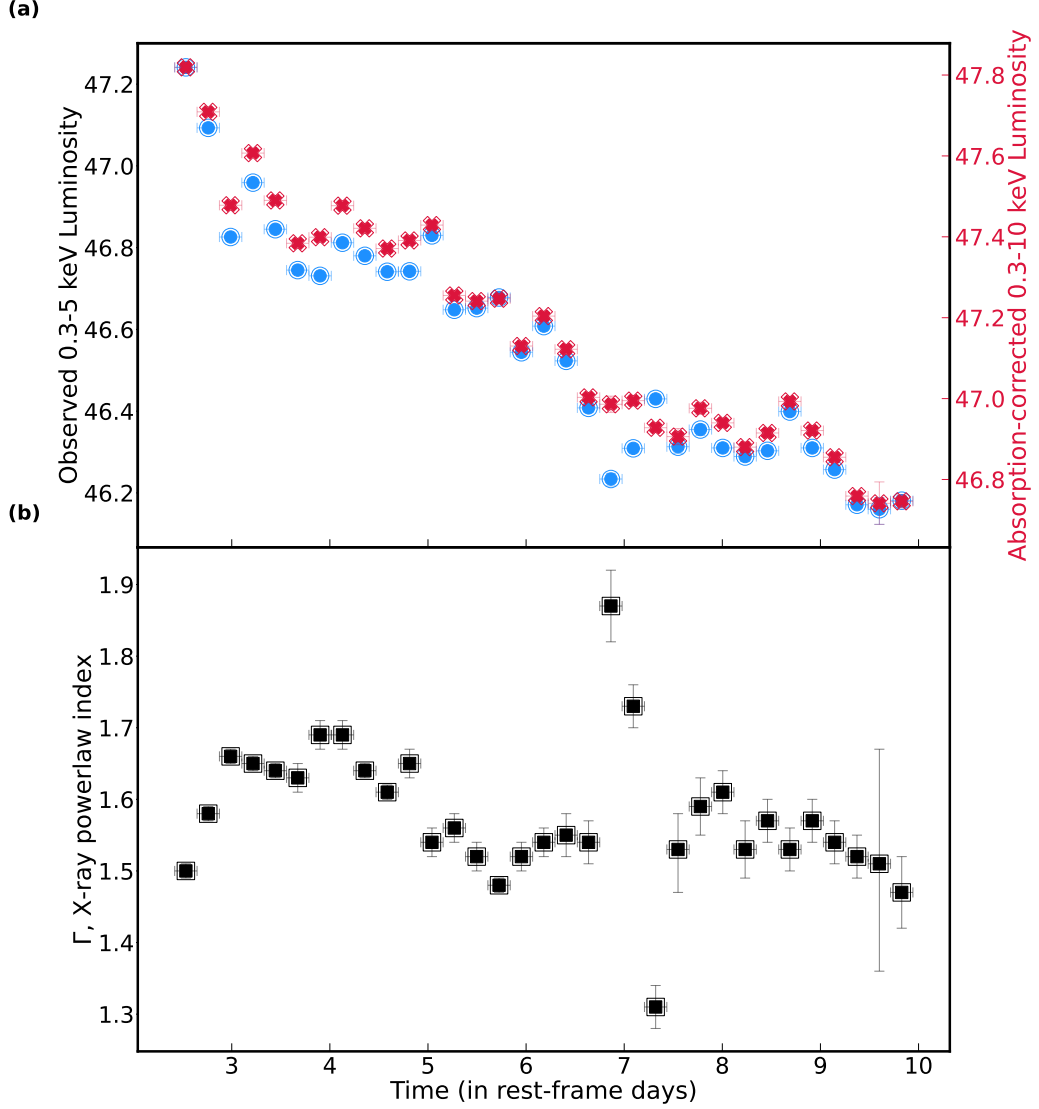
5 Estimate of gravitational lens magnification by a foreground structure

The high luminosity of AT 2022cmc motivates considering whether gravitational lensing by a foreground structure along the line of sight has magnified the flux that we detect. AT 2022cmc is located 5.6'' from the galaxy SDSS J133443.05+331305.7, at a photometric redshift of $z = 0.4 \pm 0.1$, and 3.7' from the galaxy group WHL J133453.9+331004 at a spectroscopic redshift of $z = 0.4$ (120). The optical luminosity of the group, and the sky location and colours of this

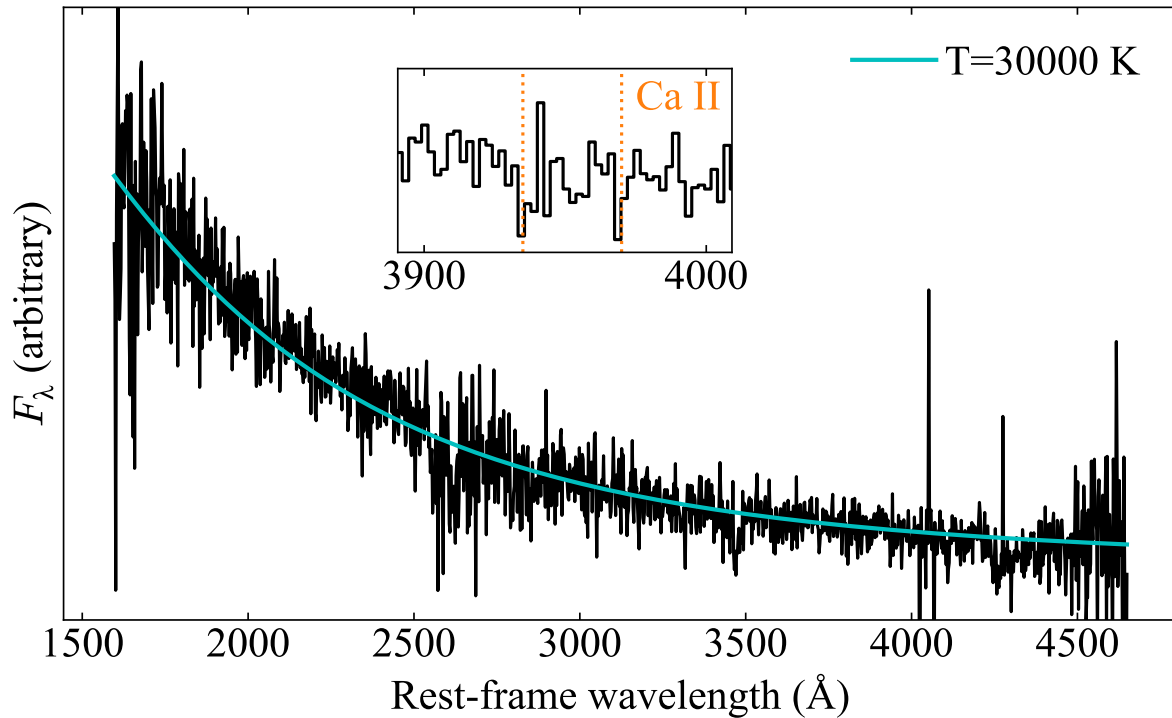
912 galaxy are consistent with our line of sight to AT 2022cmc passing adjacent to a star-forming
913 galaxy located in the infall region of ($R \simeq r_{200}$) of a galaxy group with a mass $M_{200} \simeq 3 \times$
914 $10^{13} M_{\odot}$, where the mass estimate is obtained by combining the optical luminosity from (120)
915 with the mass-observable scaling relations from (121). To estimate lens magnification by the
916 group, we assume an NFW density profile with concentration $c_{200} = 5$, and adopt the formalism
917 from (122) to estimate a magnification of $\mu \simeq 1.02$, i.e. just a $\simeq 2$ per cent magnification
918 of the flux. To estimate magnification by the galaxy, we compare its apparent magnitude in
919 red pass-bands (i.e., relatively insensitive to any ongoing star formation) with a model for a
920 passively evolving stellar population formed in a burst at a redshift of $z > 2$. This yields an
921 estimated luminosity relative to the luminosity function of cluster and group galaxies (123) of
922 $\simeq 0.3L^*$. Combining this estimate with the scaling relations between mass and luminosity
923 commonly used to estimate galaxy masses in gravitational lens models (e.g., (124)) we obtain
924 a velocity dispersion estimate for the bulge of the galaxy of $\sigma \simeq 120 \text{ km s}^{-1}$. Then, adopting a
925 singular isothermal sphere (SIS) model of the galaxy mass distribution, and using the standard
926 expressions for the lensing properties of an SIS (e.g., (125)), we derive an estimated Einstein
927 radius of $\theta_E \simeq 0.25''$ and lens magnification of $\mu \simeq 1.05$, based on the lens redshift of $z_L = 0.4$
928 and source redshift of $z_S = 1.193$. In summary, the lens magnification suffered by AT 2022cmc
929 appears to be modest at $\mu \simeq 1.05 - 1.1$, and cannot account for the high observed luminosity
930 of the X-ray to radio counterpart.



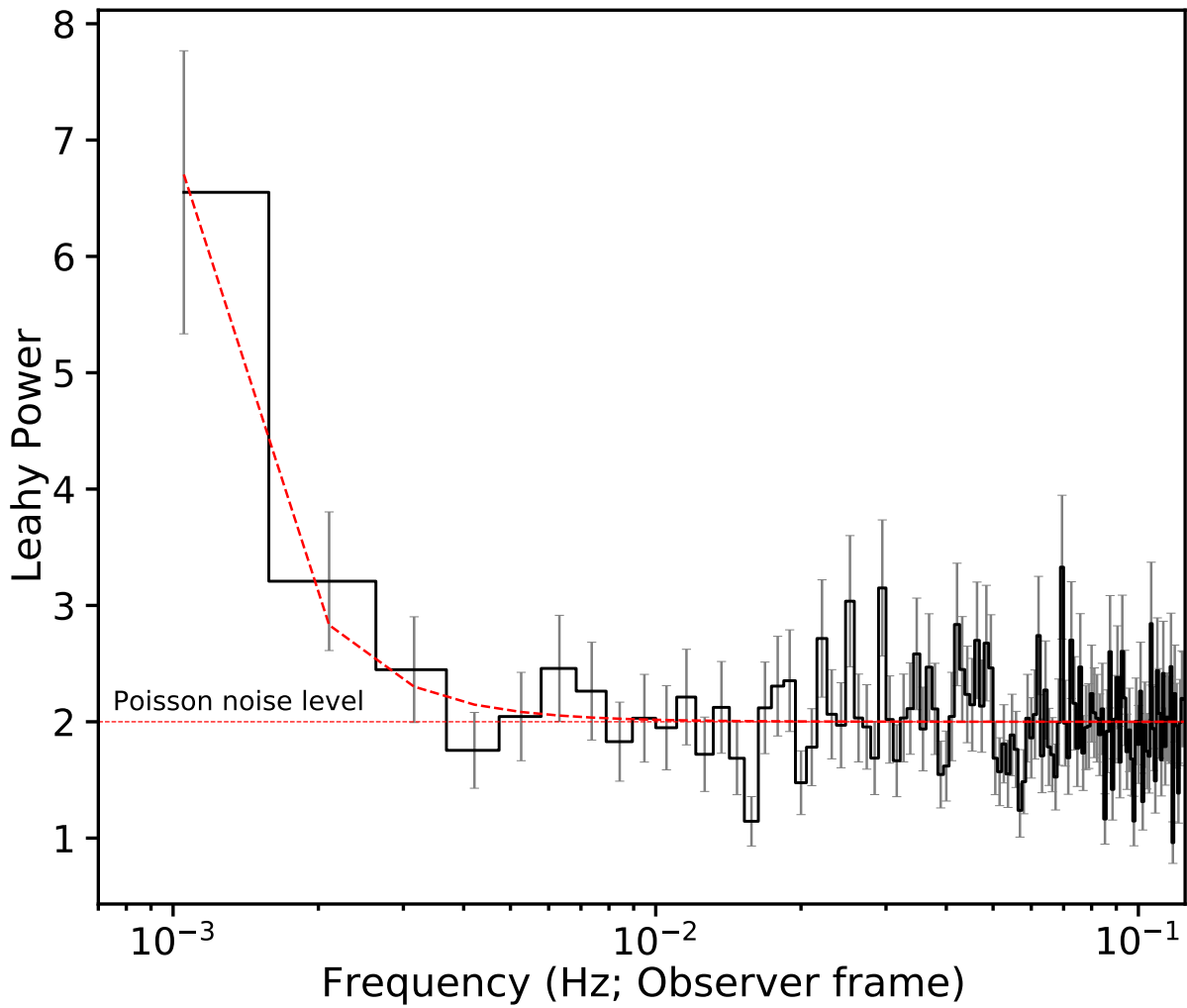
Extended Data Figure 1: *Neil Gehrels Swift XRT 0.3-8 keV image of NICER's FoV*. The yellow circle with a radius of 47'' and is centered on AT 2022cmc's radio coordinates of 13:34:43.2, +33:13:00.6 (J2000.0 epoch). The outer/dashed cyan circle shows *NICER/XTI*'s approximate field of view of 3.1' radius. There are no contaminating sources within *NICER*'s FoV. The north and east arrows are each 200'' long. The colourbar shows the number of X-ray counts.



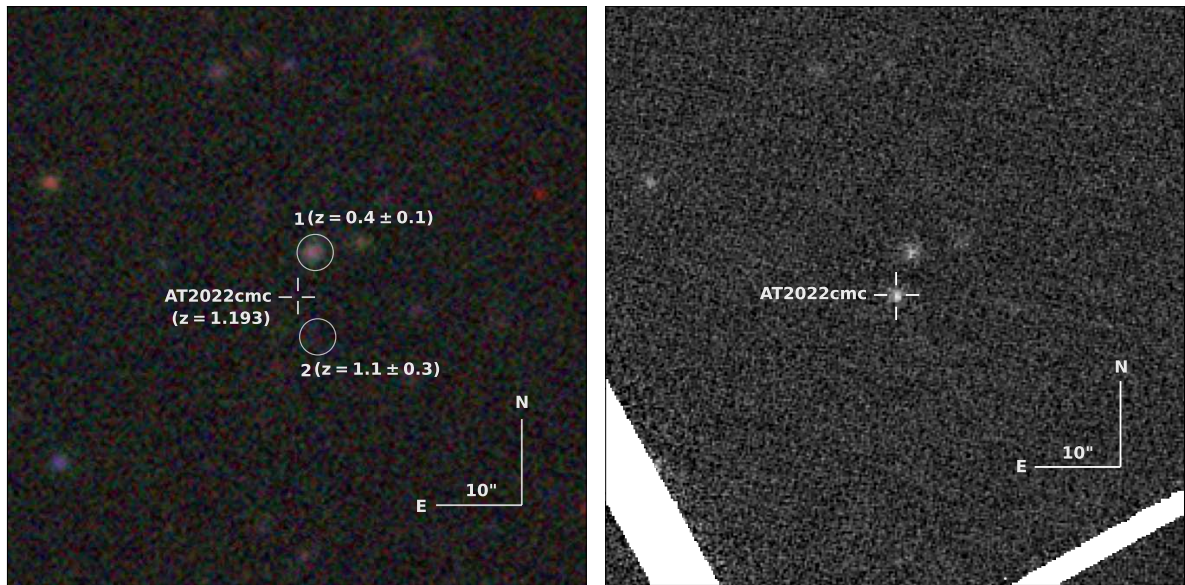
Extended Data Figure 2: **AT 2022cmc's X-ray luminosity and energy spectral slope evolution.** (a) Logarithm of the observed 0.3-5 keV (filled blue circles; left y-axis) and the absorption-corrected 0.3-10 keV luminosities (filled red crosses; right y-axis) in units of ergs s^{-1} . The errorbars on the luminosities are much smaller than the size of the data points. (b) Evolution of the best-fit power-law index with time. The abrupt changes in index around day 7 (rest-frame) coincide with a hard X-ray (2–5 keV) flare that happened during epoch E21 (the data point with best-fit photon index of ~ 1.3 ; see Extended Data Table 2). The neutral Hydrogen column of the host was tied across all epochs and the best-fit value is $(9.7 \pm 0.3) \times 10^{21} \text{ cm}^{-2}$.



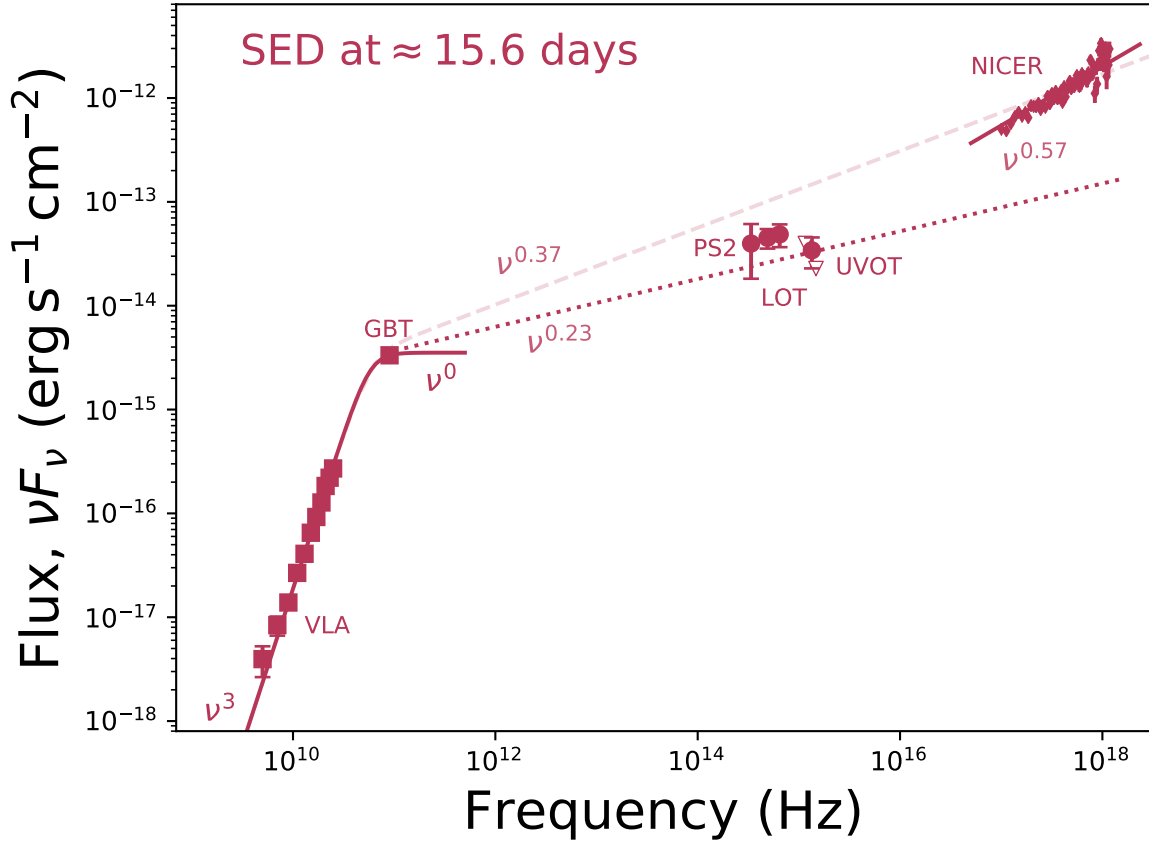
Extended Data Figure 3: **VLT/X-shooter spectrum of AT 2022cmc, obtained at ≈ 15 days after discovery.** The featureless blue continuum can be modelled with a blackbody with $T \approx 30,000$ K (solid blue line), consistent with the optical bump in the broad-band SED from day 25-27 (Figure 3). The inset shows a zoom in on the region with CaII absorption lines identified by (15).



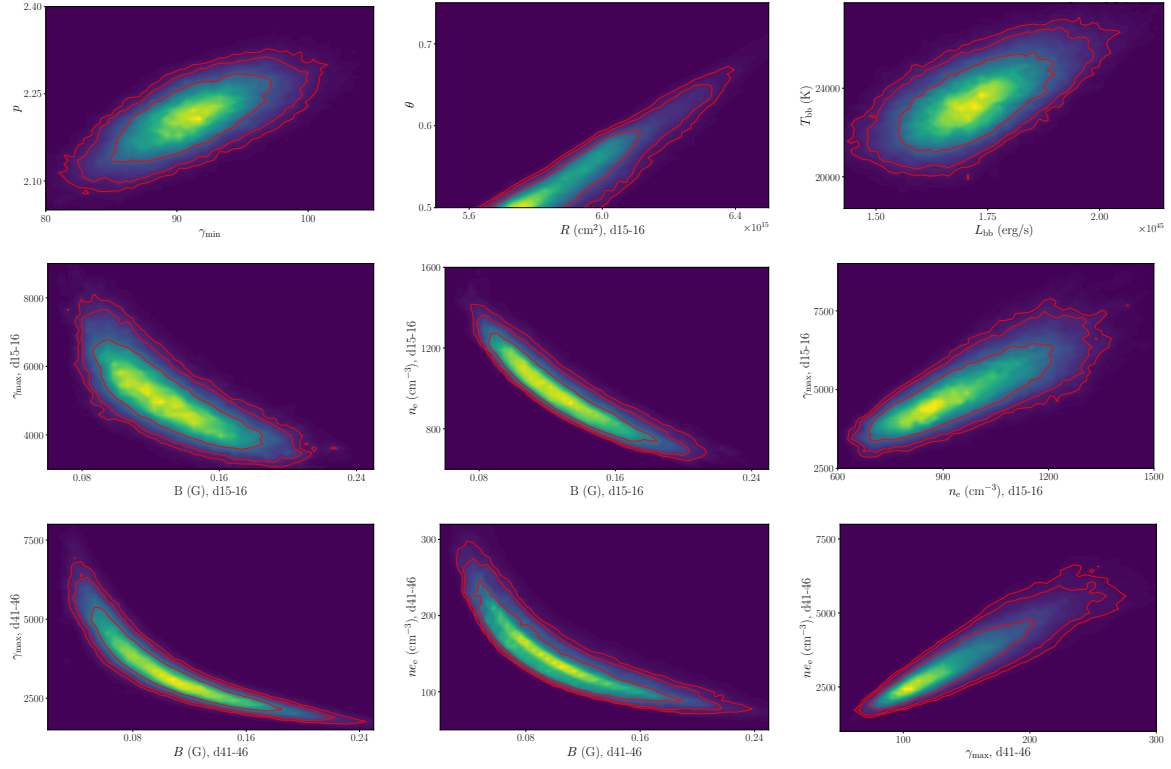
Extended Data Figure 4: **Average X-ray (0.3-5 keV) power density spectrum of AT 2022cmc.** The frequency resolution and the Nyquist frequency are 1/950 Hz and 1/8 Hz, respectively. This power spectrum is an average of 29 individual PDS. The dashed, red curve is the best-fit power-law model. Systematic variability on timescales of ~ 1000 s (lowest frequency bin) is evident. All the frequencies and hence the timescales are as measured in observer frame.



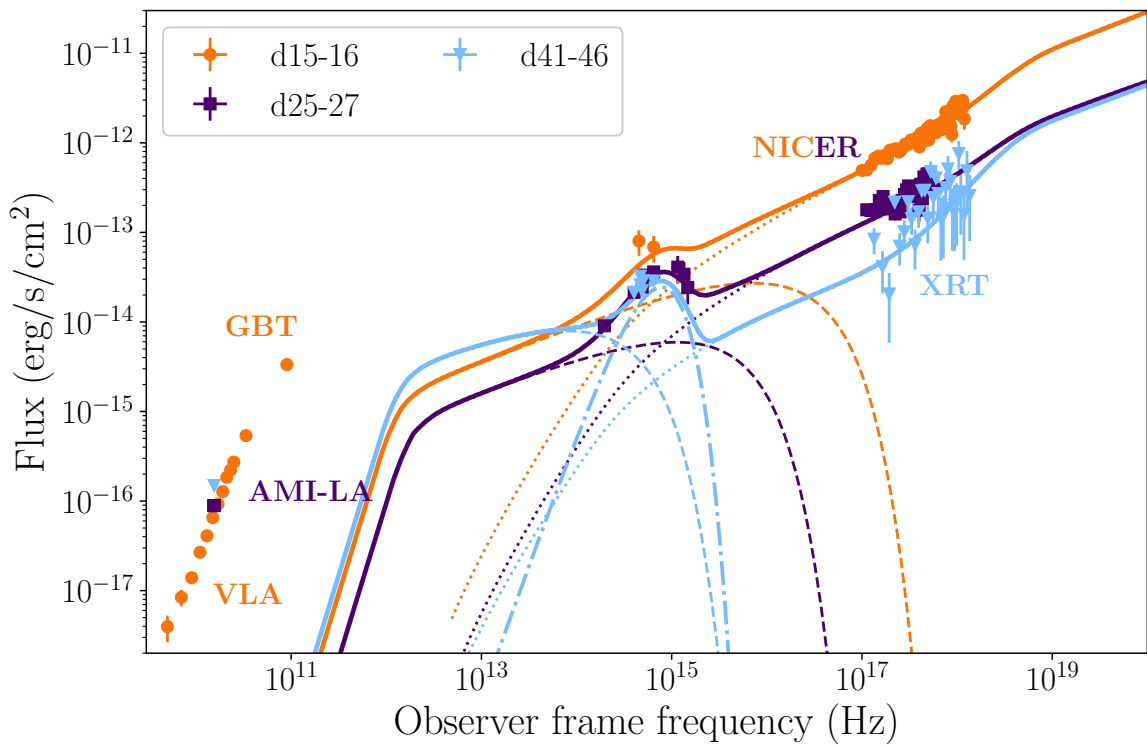
Extended Data Figure 5: Pre and post-outburst optical images of AT 2022cmc. Left panel: A colour composite image of the field prior to the outburst, made using data from the Legacy Imaging Surveys (126) using g , r and z filters. There is no emission at the location of AT 2022cmc (cross). Nearby catalogued objects with their photometric redshifts are shown (circles). Right panel: A PS2 w -band image of AT 2022cmc post outburst. The size of both image cutouts is $1.1' \times 1.1'$. North and the East arrows are each $10''$.



Extended Data Figure 6: **Spectral energy distribution of AT 2022cmc at ≈ 15.6 days after discovery.** Data at radio (VLA), mm-band (GBT), UV/optical (*Swift*/UVOT, ZTF, PanSTARRS) and X-ray frequencies (*NICER*), demonstrate that the SED at this time cannot be explained as a single synchrotron spectrum. The SED at $\lesssim 25$ GHz is optically thick ($\nu F_\nu \propto \nu^3$), with a spectral break near ≈ 90 GHz. The spectral index from the GBT observation at ≈ 90 GHz to the *NICER* band is $\nu F_\nu \propto \nu^{0.37}$, which (i) is significantly shallower than the observed *NICER* spectral index ($\nu F_\nu \propto \nu^{0.57}$) and (ii) significantly over-predicts the UV flux at this time.



Extended Data Figure 7: **Contour plots for the best-fitting parameters of model 1.** For clarity, we only show the 2d posterior distributions of parameters that are degenerate with each other.



Extended Data Figure 8: **Best fitting External inverse Compton (EC) model.** The EC model requires a jet that under-predicts the radio flux. Furthermore, EC produces too little soft X-ray flux, and as in model 1 the emission at these frequencies is dominated by SSC.

Extended Data Table 1: **The first few entries of the multi-wavelength data presented in this work.** The entire dataset can be found in machine-readable format in the supplementary file named “allphot.txt”. The **Time** column lists days in observer frame since MJD 59621.4458. All optical/UV photometry (**Flux** in milliJansky) has been corrected for MilkyWay extinction. AT 2022cmc’s host galaxy was not detected in the pre-explosion panSTARRs images so host-subtraction was not performed. **Observatory** is the name of the facility. Values of 1 and 0 in the “Detection” column indicate flux measurements and 3σ upper limits, respectively.

The first few entries of the multi-wavelength data presented in this work.								
Time (days)	Observatory	Instrument	Filter	Frequency (Hz)	Flux (mJy)	Flux Error (mJy)	Detection? (1=Yes)	data source
1.03×10^0	ATLAS	NA	o	4.52×10^{14}	8.93×10^{-2}	8.62×10^{-3}	1	This work
1.05×10^0	ZTF	NA	g'	6.46×10^{14}	5.93×10^{-2}	3.37×10^{-3}	1	This work
1.07×10^0	ZTF	NA	r'	4.90×10^{14}	8.71×10^{-2}	3.27×10^{-3}	1	This work
2.07×10^0	ATLAS	NA	o	4.52×10^{14}	5.05×10^{-2}	6.42×10^{-3}	1	This work
.
.
.
.

Extended Data Table 2: **Summary of time-resolved X-ray energy spectral modeling of AT 2022cmc.** Here, 0.3-5.0 keV *NICER* spectra are fit with *tbabs***ztbabs***zashift*(*clumin***pow*) model using *XSPEC* (45). **Start** and **End** represent the start and end times (in units of MJD) of the interval used to extract a combined *NICER* spectrum. **Exposure** is the accumulated exposure time during this time interval. **FPMs:** The total number of active detectors minus the “hot” detectors. **Phase** is the name used to identify the epoch. **Index** is the photon index of the power law component. **Log(Integ. Lum.)** is the logarithm of the integrated absorption-corrected power law luminosity in 0.3-10 keV in units of erg s⁻¹. **Log(Obs. Lum.)** is the logarithm of the observed 0.3-5.0 keV luminosity in units of erg s⁻¹. **Count Rate** is the background-subtracted *NICER* count rate in 0.3-5.0 keV in units of counts/sec/FPM. All errorbars represent 1- σ uncertainties. χ^2/bins represents the best-fit χ^2 and the number of spectral bins. The total $\chi^2/\text{degrees of freedom}$ is 2135.3/1956.

Best-fit parameters from fitting time-resolved 0.3-5.0 keV <i>NICER</i> X-ray spectra									
Start (MJD)	End (MJD)	Exposure (ks)	FPMs	Phase	Index	Log(Integ. Lum.) (0.3-10 keV)	Log(Obs. Lum.) (0.3-5.0 keV)	Count rate (0.3-5.0 keV)	χ^2/bins
59626.75	59627.25	6.36	52	E0	$1.5^{+0.01}_{-0.01}$	$47.825^{+0.003}_{-0.003}$	$47.247^{+0.003}_{-0.002}$	0.2354 ± 0.0011	68.3/77
59627.25	59627.75	5.28	52	E1	$1.58^{+0.01}_{-0.01}$	$47.715^{+0.004}_{-0.004}$	$47.099^{+0.002}_{-0.004}$	0.1733 ± 0.0011	97.4/73
59627.75	59628.25	4.8	52	E2	$1.66^{+0.01}_{-0.01}$	$47.484^{+0.005}_{-0.005}$	$46.832^{+0.002}_{-0.004}$	0.0971 ± 0.001	112.6/72
59628.25	59628.75	5.76	52	E3	$1.65^{+0.01}_{-0.01}$	$47.613^{+0.004}_{-0.004}$	$46.965^{+0.004}_{-0.002}$	0.1309 ± 0.001	70.0/73
59628.75	59629.25	3.48	52	E4	$1.64^{+0.01}_{-0.01}$	$47.496^{+0.006}_{-0.006}$	$46.851^{+0.004}_{-0.004}$	0.1008 ± 0.0013	83.7/71
59629.25	59629.75	2.28	52	E5	$1.63^{+0.02}_{-0.02}$	$47.39^{+0.008}_{-0.008}$	$46.751^{+0.006}_{-0.005}$	0.0801 ± 0.0019	58.3/66
59629.75	59630.25	2.64	52	E6	$1.69^{+0.02}_{-0.02}$	$47.405^{+0.008}_{-0.008}$	$46.737^{+0.006}_{-0.004}$	0.0792 ± 0.0018	70.4/67
59630.25	59630.75	2.76	51	E7	$1.69^{+0.02}_{-0.02}$	$47.483^{+0.007}_{-0.007}$	$46.818^{+0.005}_{-0.004}$	0.0954 ± 0.0017	64.2/69
59630.75	59631.25	3.84	52	E8	$1.64^{+0.01}_{-0.01}$	$47.427^{+0.006}_{-0.006}$	$46.786^{+0.004}_{-0.006}$	0.0865 ± 0.0014	63.0/71
59631.25	59631.75	5.64	52	E9	$1.61^{+0.01}_{-0.01}$	$47.377^{+0.005}_{-0.005}$	$46.747^{+0.004}_{-0.003}$	0.0785 ± 0.0009	86.8/72
59631.75	59632.25	2.76	52	E10	$1.65^{+0.02}_{-0.02}$	$47.397^{+0.007}_{-0.007}$	$46.748^{+0.004}_{-0.004}$	0.0801 ± 0.0017	69.5/68
59632.25	59632.75	3.72	52	E11	$1.54^{+0.02}_{-0.02}$	$47.436^{+0.007}_{-0.007}$	$46.836^{+0.005}_{-0.006}$	0.0696 ± 0.0012	73.1/71
59632.75	59633.25	3.36	52	E12	$1.56^{+0.02}_{-0.02}$	$47.261^{+0.007}_{-0.007}$	$46.654^{+0.005}_{-0.006}$	0.0621 ± 0.0014	66.2/68
59633.25	59633.75	3.12	52	E13	$1.52^{+0.02}_{-0.02}$	$47.247^{+0.007}_{-0.007}$	$46.658^{+0.005}_{-0.005}$	0.0617 ± 0.0014	74.5/68
59633.75	59634.25	6.36	52	E14	$1.48^{+0.01}_{-0.01}$	$47.253^{+0.005}_{-0.005}$	$46.684^{+0.003}_{-0.003}$	0.0643 ± 0.0008	71.4/72
59634.25	59634.75	4.44	52	E15	$1.52^{+0.02}_{-0.02}$	$47.136^{+0.007}_{-0.007}$	$46.55^{+0.007}_{-0.006}$	0.048 ± 0.001	79.7/69
59634.75	59635.25	2.28	52	E16	$1.54^{+0.02}_{-0.02}$	$47.21^{+0.009}_{-0.009}$	$46.614^{+0.006}_{-0.007}$	0.056 ± 0.0019	62.5/63
59635.25	59635.75	1.8	52	E17	$1.55^{+0.03}_{-0.03}$	$47.128^{+0.007}_{-0.007}$	$46.529^{+0.008}_{-0.008}$	0.0463 ± 0.0024	50.6/58
59635.75	59636.25	2.16	52	E18	$1.54^{+0.03}_{-0.03}$	$47.009^{+0.011}_{-0.011}$	$46.414^{+0.008}_{-0.011}$	0.0355 ± 0.002	45.3/58
59636.25	59636.75	1.2	52	E19	$1.87^{+0.05}_{-0.05}$	$46.992^{+0.02}_{-0.02}$	$46.24^{+0.013}_{-0.013}$	0.0272 ± 0.0033	32.4/40
59636.75	59637.25	2.52	52	E20	$1.73^{+0.03}_{-0.03}$	$47.001^{+0.013}_{-0.013}$	$46.315^{+0.01}_{-0.006}$	0.0306 ± 0.0016	50.2/54
59637.25	59637.75	2.28	52	E21	$1.31^{+0.03}_{-0.03}$	$46.934^{+0.011}_{-0.011}$	$46.436^{+0.013}_{-0.01}$	0.0349 ± 0.0018	125.5/62
59637.75	59638.25	0.84	52	E22	$1.53^{+0.06}_{-0.05}$	$46.912^{+0.02}_{-0.02}$	$46.319^{+0.016}_{-0.015}$	0.0288 ± 0.0053	34.9/39
59638.25	59638.75	1.44	49	E23	$1.59^{+0.04}_{-0.04}$	$46.982^{+0.015}_{-0.015}$	$46.361^{+0.013}_{-0.008}$	0.0322 ± 0.0029	33.5/47
59638.75	59639.25	2.88	52	E24	$1.61^{+0.03}_{-0.03}$	$46.946^{+0.011}_{-0.011}$	$46.317^{+0.01}_{-0.006}$	0.0293 ± 0.0015	64.2/60
59639.25	59639.75	2.4	49	E25	$1.53^{+0.04}_{-0.04}$	$46.886^{+0.013}_{-0.013}$	$46.295^{+0.007}_{-0.007}$	0.0272 ± 0.0017	58.0/56
59639.75	59640.25	3.12	52	E26	$1.57^{+0.03}_{-0.03}$	$46.921^{+0.011}_{-0.011}$	$46.31^{+0.009}_{-0.006}$	0.0284 ± 0.0013	66.2/59
59640.25	59640.75	2.76	52	E27	$1.53^{+0.03}_{-0.03}$	$46.999^{+0.011}_{-0.011}$	$46.405^{+0.008}_{-0.01}$	0.0347 ± 0.0015	48.6/59
59640.75	59641.25	2.64	49	E28	$1.57^{+0.03}_{-0.03}$	$46.927^{+0.012}_{-0.012}$	$46.316^{+0.009}_{-0.009}$	0.0286 ± 0.0014	42.5/56
59641.25	59641.75	3.0	52	E29	$1.54^{+0.03}_{-0.03}$	$46.861^{+0.012}_{-0.012}$	$46.263^{+0.009}_{-0.012}$	0.0252 ± 0.0012	63.7/56
59641.75	59642.25	4.44	52	E30	$1.52^{+0.03}_{-0.03}$	$46.765^{+0.011}_{-0.011}$	$46.177^{+0.01}_{-0.007}$	0.0206 ± 0.0009	66.0/61
59642.25	59642.75	0.24	52	E31	$1.51^{+0.15}_{-0.16}$	$46.747^{+0.052}_{-0.053}$	$46.166^{+0.042}_{-0.035}$	0.0208 ± 0.0175	11.8/12
59642.75	59643.25	2.4	48	E32	$1.47^{+0.05}_{-0.05}$	$46.752^{+0.016}_{-0.016}$	$46.187^{+0.014}_{-0.011}$	0.021 ± 0.0019	70.5/56

Extended Data Table 3: **Summary of the best-fitting jet models.** The emitting region magnetic field B , radius R and number density n_e , as well as the maximum Lorentz factor of the particles γ_{\max} were left free to vary in each epoch. The minimum electron Lorentz factor γ_{\min} , particle distribution slope p , jet bulk Lorentz factor Γ_j , viewing angle θ , black body luminosity L_{bb} and black body temperature T_{bb} were tied. The parameters marked with a * were pegged to their limit. The statistic for the overall joint fit is $\chi^2/\text{d.o.f.} = 305.54/138 = 2.20$ for model 1 and $284.45/123 = 2.31$ for model 2. We also report the power carried by the electrons, protons (assuming one cold proton per electron) and magnetic field P_e , P_p , P_b , the total jet power $P_j = P_e + P_p + P_b$, the equipartition fraction U_e/U_b , and the black body radius R_{bb} .

Model 1	59636.446 - 59638.446	59636.446 - 59638.446	59662.446 - 59667.446	Tied
B (G)	$0.13^{+0.03}_{-0.03}$	$1.0^{+0.2}_{*} \times 10^{-2}$	$9.7^{+5.4}_{-3.5} \times 10^{-2}$	
R (cm)	$5.9^{+0.2}_{-0.1} \times 10^{15}$	$6.9^{+0.3}_{-0.3} \times 10^{15}$	$1.0^{*}_{-0.3} \times 10^{16}$	
n_e (cm $^{-3}$)	973^{+195}_{-160}	2200^{+237}_{-205}	144^{+58}_{-38}	
γ_{\max}	$5.0^{+1.2}_{-0.9} \times 10^3$	$3.2^{+1.8}_{-0.4} \times 10^4$	$3.4^{+1.4}_{-0.9} \times 10^3$	
γ_{\min}				91^{+4}_{-4}
p				$2.21^{+0.05}_{-0.05}$
Γ_j				86^{+9}_{-10}
θ				$0.5^{+0.1}_{*}$
L_{bb} (erg/s)				$1.71^{+0.13}_{-0.11} \times 10^{45}$
T_{bb} (K)				$2.34^{+0.16}_{-0.14} \times 10^4$
δ				103
P_e (erg/s)	5.3×10^{45}	2.0×10^{46}	2.0×10^{45}	
P_b (erg/s)	1.6×10^{43}	1.5×10^{41}	2.6×10^{43}	
P_p (erg/s)	3.6×10^{46}	1.1×10^{47}	1.5×10^{46}	
P_j (erg/s)	4.1×10^{46}	1.3×10^{47}	1.7×10^{46}	
U_e/U_b	325	1.3×10^5	77	
R_{bb} (cm)				2.8×10^{15}
Model 2	59636.446 - 59638.446	59636.446 - 59638.446	59662.446 - 59667.446	Tied
B (G)	$10.2^{+2.0}_{-1.6}$	18^{+5}_{-3}	36^{+14}_{-9}	
R (cm)	$1.16^{+0.12}_{-0.10} \times 10^{14}$	$6.0^{+0.9}_{-0.8} \times 10^{13}$	$2.2^{+0.4}_{-0.6} \times 10^{14}$	
n_e (cm $^{-3}$)	$8.7^{+1.5}_{-1.3} \times 10^7$	$1.3^{+0.3}_{-0.3} \times 10^8$	$4.2^{+2.0}_{-1.5} \times 10^6$	
γ_{\max}	$1.2^{+0.9}_{-0.4} \times 10^4$	$3.4^{+2.2}_{-1.3} \times 10^3$	$6.7^{+2.3}_{-1.7} \times 10^2$	
γ_{\min}				$4.7^{+0.5}_{-0.4}$
p				$2.13^{+0.09}_{-0.08}$
Γ_j				5^{+1}_{-*}
θ				$1.3^{+0.8}_{-0.6}$
L_{bb} (erg/s)				$1.36^{+0.10}_{-0.08} \times 10^{45}$
T_{bb} (K)				$2.10^{+0.11}_{-0.10} \times 10^4$
δ				10.7
P_e (erg/s)	4.5×10^{43}	2.3×10^{43}	7.6×10^{42}	
P_b (erg/s)	1.6×10^{41}	1.4×10^{41}	6.9×10^{42}	
P_p (erg/s)	5.0×10^{45}	2.0×10^{45}	8.2×10^{44}	
P_j (erg/s)	5.1×10^{45}	2.0×10^{45}	8.4×10^{44}	
U_e/U_b	412	164	1.1	
R_{bb} (cm)				3.1×10^{15}

Supplementary Files

This is a list of supplementary files associated with this preprint. Click to download.

- [allphot.txt](#)
- [Fig1data.tar](#)
- [nicertimeresolvedspectralfits.txt](#)